Frequency Response Expansion Strategy for Nonlinear Structures

Xing Wang, Thomas L. Hill, Simon A. Neild

Department of Mechanical Engineering, University of Bristol, Bristol BS8 1TR, United Kingdom

Abstract

Finite-element (FE) models of engineering structures are generally of high order to provide detailed descriptions of the structure's static and dynamic response. However, experimental testing of such structures can only obtain spatially-incomplete sets of response data. For linear structures, the response of unmeasured degrees-of-freedom (DOFs) can be estimated using linear expanded mode shapes and experimentally-extracted linear modal parameters. Nevertheless, such techniques cannot be directly applied to nonlinear structures when the responses are distorted when driven by high levels of excitation and modal superposition is no longer valid. This paper presents a novel strategy to expand spatially-incomplete measured data to the FE-modelled DOFs that is suitable for nonlinear structures. This strategy is an extension of the current linear expansion techniques; it starts with linear experimental modal analysis and conventional linear expansion technique to estimate the unmeasured responses of the underlying linear system using low-amplitude testing data. Then the nonlinear responses, measured during high-amplitude testing, are correlated with the measured underlying linear dynamics to extract the residuals, which are subsequently used to estimate the nonlinear stiffness and damping coefficients. Finally, the unmeasured nonlinear responses are expanded using the modal properties from linear experimental analysis and estimated nonlinear coefficients. The strategy is validated using two case studies: the first is a numerical two-beam example with a localised nonlinear spring; the second is an asymmetric diesis-like structure with geometrical nonlinearities, in which data from experimental testing are used.

Keywords: frequency response expansion, spatially-incomplete measurement, nonlinear structure

1. Introduction

Structures are routinely assumed to be linear during the design and test process, although nonlinear behaviours, such as resonance frequency shifts [1,2] or differences in mode shapes driven by multiple levels of inputs [3,4], are occasionally observed during, for example, ground vibration testing of an aircraft. These behaviours are accounted for by assigning a large safety factor (sometimes called model factor) to a reference linear model and thereby results in a conservative design [5]. However, due to a continuous demand for more efficient and lighter-weight structures, the actual structural behaviour can be far from linear, resulting in unreliable estimation of safety factors or even failure. For such structures, it is preferable to incorporate the nonlinear dynamics in the model to capture the critical nonlinear phenomena observed during testing and to improve the prediction fidelity of its mathematical model [6-10].

This paper focuses on the issue of spatially-incomplete measurement during testing. A finite-element model generally contains detailed geometric features and many DOFs; however, only a subset of these DOFs are measured during a test. This is due to the limited number of measurement channels, inaccessible locations as well as difficulties in measuring rotational DOFs. For linear structures, this problem can be resolved by reducing the finite-element model to the measured region [11] or expanding the measured data - frequency response functions (FRFs) [12] or mode shapes [13,14] - to the analytically-modelled region using modal decoupling and superposition techniques. Nevertheless, these techniques are not valid for nonlinear structures. One challenge is that nonlinear structures have input-dependent FRFs, and so the nonlinear parameters should be estimated before employing an expansion technique to capture this key feature. An effective approach is to use the frequency-domain nonlinear subspace identification procedure [15,16], where the nonlinear forces are regarded as feedback forces to the underlying linear system; it requires direct measurements at all locations where nonlinearities exist. Achieving this requirement is not always possible in practice, especially when the nonlinearities are distributed. An alternative approach is to extract modal properties using a dedicated nonlinear phase resonance testing technique and then synthesise the nonlinear frequency responses at measured DOFs using the nonlinear modes, as demonstrated for structures with isolated resonances by Peter et al. [17]. For a nonlinear structure with closely-spaced underlying linear modes, the nonlinear responses are complex - for

example, the deflection shapes may alter significantly during testing [18] - which makes it very difficult to isolate one mode and perform the phase resonance testing. In this respect, this paper proposes a response expansion strategy to expand the measured nonlinear responses to the entire FE-modelled region. It utilises low-amplitude test data to update the FE model of the underlying linear system and perform a linear expansion using mature techniques. High-amplitude data from standard stepped-sine or swept-sine testing techniques are then used to estimate the nonlinear parameters and perform the expansion. The strategy is first demonstrated with a numerical model of two beams connected with a discrete nonlinear spring. It is then applied to the experimentally-measured data of an asymmetric, diesis-like structure with geometrical nonlinearities.

The rest of the paper is structured as follows: in Section 2, we derive the expansion strategy; Section 3 describes a numerical example of a two-beam model with a discrete nonlinear spring; the experimental testing of an asymmetric diesis-like structure with geometrical nonlinearities is then discussed in Section 4. Finally, conclusions are drawn in Section 5.

2. Theoretical background

2.1. General framework and dynamic equations

A typical measurement of a nonlinear structure can be divided into two sets of testing: low-amplitude and high-amplitude tests [19,20]. It is assumed that homogeneous FRFs, i.e., FRFs that are independent of the input spectrum [21], are obtained using low-amplitude random or sinusoidal testing and thereby the measured responses can be expanded to unmeasured regions using mature linear expansion theory [12-14]. A finite-element model of the underlying linear part of the structure is assumed to be available in the proposed nonlinear expansion technique. High-amplitude tests, e.g., stepped-sine or slowly-swept-sine excitations, drive the structure to its operational energy level where significant nonlinear distortions may be observed in the responses. This testing procedure for a nonlinear structure is appealing because the data can be obtained using conventional testing equipment in industry. This paper aims to extend the linear expansion technique to incorporate high-amplitude test data in which nonlinear behaviour is

observed. Here, the measured responses are assumed to be periodic and the primary harmonic term is considered to be the dominant component, as is observed in many engineering structures [1-3,10,19,20]. Additional resonances such as the sub- and/or super-harmonic resonances are assumed to be negligible. More complicated nonlinear responses such as quasi-periodic or chaotic motions are not within the scope of the expansion technique discussed here.

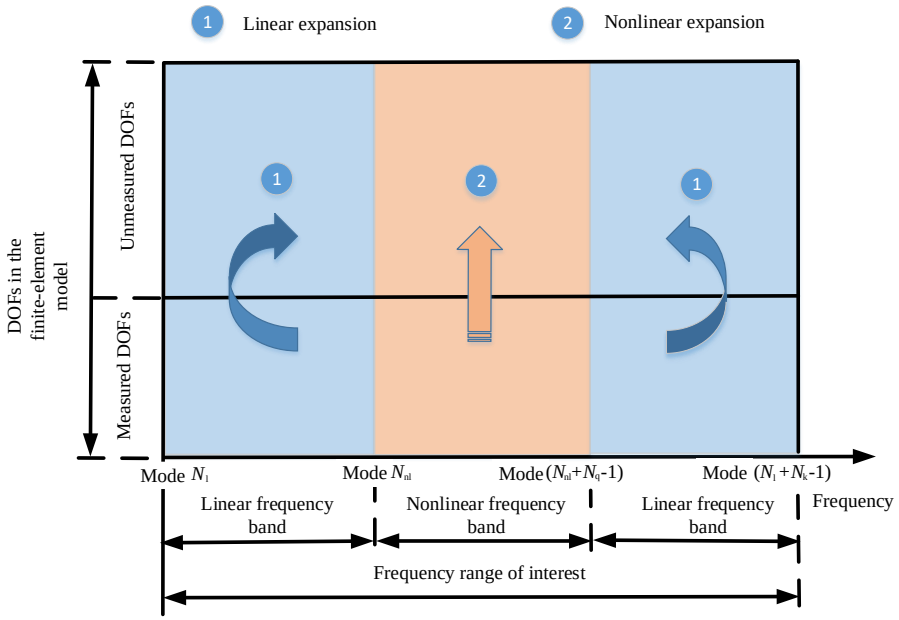

Fig. 1. Illustration of frequency response expansion techniques used for a nonlinear structure.

As shown in Fig. 1, the response of a nonlinear structure during high-amplitude testing can be divided into *linear frequency band* (frequency bandwidth where FRFs are approximately homogeneous using multiple input forcing levels) and *nonlinear frequency band* (frequency bandwidth where homogeneous FRFs are observed using low-amplitude testing and distortions such as amplitude-dependent FRFs or jumps occur using high-amplitude testing). In the linear frequency band, the modal parameters of the nonlinear structure remain unchanged in the high-amplitude testing, i.e. the modes are not noticeably affected by nonlinearities, thus the mature linear expansion technique [12] can be applied for the data in this frequency range. On the other hand, the responses in the nonlinear frequency band require a nonlinear expansion technique, which is the main focus of this paper. The expansion techniques used in the proposed expansion strategy for a nonlinear structure are summarised in Table 1.

The proposed nonlinear expansion technique makes use of the following assumptions: 1) it is performed after the linear expansion using data from low-amplitude testing; 2) it can utilise the linear modal parameters and linear expanded data, i.e., the underlying linear responses of the unmeasured DOFs are obtained prior to the nonlinear expansion; 3) the modes outside the nonlinear frequency band are approximately linear and can be pre-identified using data from the low-amplitude testing. With these assumptions, the nonlinear expansion strategy is shown in Fig. 2.

Table 1

Expansion techniques used in the proposed expansion strategy for a nonlinear structure

Amplitude of input force	Frequency range of interest	
	Linear frequency band	Nonlinear frequency band
Low-amplitude	Linear expansion technique [12-14]	Linear expansion technique [12-14]
High-amplitude	Linear expansion technique [12-14]	Nonlinear expansion technique

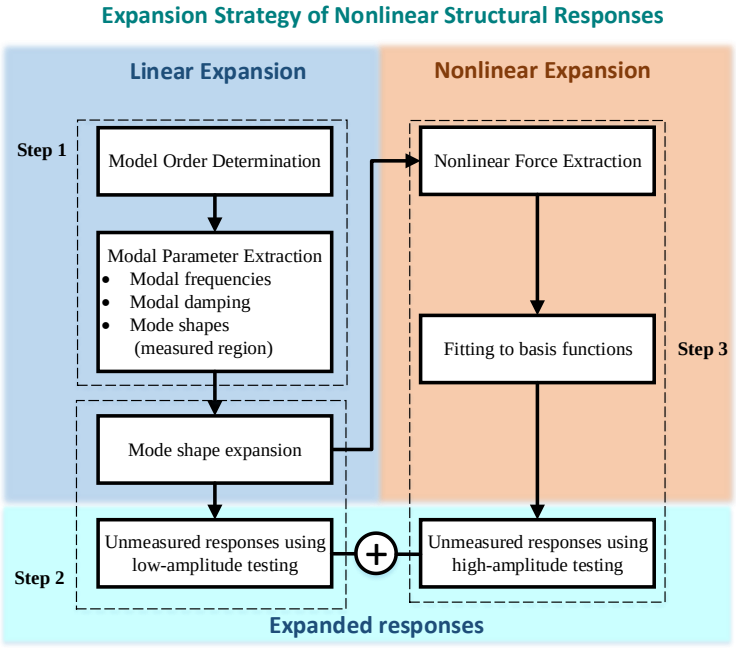

Fig. 2. Flowchart of the proposed frequency response expansion strategy for a nonlinear structure.

In order to describe the expansion technique, we consider the governing equation of an *N*-DOF nonlinear structure

$$\mathbf{M}\ddot{\boldsymbol{x}} + \mathbf{C}\dot{\boldsymbol{x}} + \mathbf{K}\boldsymbol{x} + \boldsymbol{f}\left(\boldsymbol{x}, \dot{\boldsymbol{x}}\right) = \boldsymbol{p}(t), \tag{1}$$

where matrices $\mathbf{M}$, $\mathbf{C}$, $\mathbf{K} \in \mathbb{R}^{N\times N}$ denote the linear mass, damping, and stiffness, respectively. Vectors $\boldsymbol{x}$, $\dot{\boldsymbol{x}}$, $\ddot{\boldsymbol{x}} \in \mathbb{R}^{N\times 1}$ denote the displacement, velocity, and acceleration, respectively. Vector $\boldsymbol{f}\left(\boldsymbol{x},\dot{\boldsymbol{x}}\right) \in \mathbb{R}^{N\times 1}$ contains the nonlinear force and vector $\boldsymbol{p}(t) \in \mathbb{R}^{N\times 1}$ denotes the applied force, which we take to be a single harmonic excitation such that

$$\boldsymbol{p}(t) = \mathrm{Im}\left(\boldsymbol{P}\mathrm{e}^{\mathrm{j}\omega t}\right), \tag{2}$$

where $\boldsymbol{P} \in \mathbb{C}^{N\times 1}$ is the complex amplitude of $\boldsymbol{p}(t)$, ω is the frequency of the harmonic excitation. j is the imaginary unit.

Recall that we assume the responses of the structure are dominated by their primary harmonic terms, i.e., the contribution of higher order harmonics are comparably small and can be neglected [1-3,10,19,20], As such, we denote

$$\boldsymbol{x}(t) = \mathrm{Im}\left(\boldsymbol{X}\mathrm{e}^{\mathrm{j}\omega t}\right) \quad \text{and} \quad \boldsymbol{f}(t) = \mathrm{Im}\left(\boldsymbol{F}\mathrm{e}^{\mathrm{j}\omega t}\right), \tag{3}$$

where $\boldsymbol{X}$, $\boldsymbol{F} \in \mathbb{C}^{N\times 1}$ are complex amplitudes of the primary harmonic terms of $\boldsymbol{x}(t)$ and $\boldsymbol{f}(t)$, respectively. Note that the frequency spectrum of the responses should be carefully monitored in testing to ensure that the primary harmonic assumption is reasonable. This is generally true for a nonlinear structure responding near its resonances [10,19,20].

Following the assumption of Eqs. (2) and (3) and grouping the primary harmonic terms in Eq. (1) gives

$$\left(-\omega^2\mathbf{M} + \mathrm{j}\omega\mathbf{C} + \mathbf{K}\right)\boldsymbol{X} + \boldsymbol{F}\left(\boldsymbol{X}, \mathrm{j}\omega\boldsymbol{X}\right) = \boldsymbol{P}. \tag{4}$$

Introducing the linear receptance matrix $\mathbf{H} \in \mathbb{C}^{N\times N}$ as

$$\mathbf{H} = \left(-\omega^2\mathbf{M} + \mathrm{j}\omega\mathbf{C} + \mathbf{K}\right)^{-1}, \tag{5}$$

and pre-multiplying both sides of Eq. (4) by $\mathbf{H}$, we obtain the expression of nonlinear responses as

$$\boldsymbol{X} = \mathbf{H}\boldsymbol{P} - \mathbf{H}\boldsymbol{F}\left(\boldsymbol{X}, \mathrm{j}\omega\boldsymbol{X}\right). \tag{6}$$

Note that only a subset of DOFs can be measured during testing, we thereby partition Eq. (6) into measured and unmeasured regions giving

$$\begin{Bmatrix} \boldsymbol{X}_m \\ \boldsymbol{X}_u \end{Bmatrix} = \begin{bmatrix} \mathbf{H}_{mm} & \mathbf{H}_{mu} \\ \mathbf{H}_{um} & \mathbf{H}_{uu} \end{bmatrix} \begin{Bmatrix} \boldsymbol{P}_m \\ \boldsymbol{P}_u \end{Bmatrix} - \begin{bmatrix} \mathbf{H}_{mm} & \mathbf{H}_{mu} \\ \mathbf{H}_{um} & \mathbf{H}_{uu} \end{bmatrix} \begin{Bmatrix} \boldsymbol{F}_m\left(\boldsymbol{X}, \mathrm{j}\omega\boldsymbol{X}\right) \\ \boldsymbol{F}_u\left(\boldsymbol{X}, \mathrm{j}\omega\boldsymbol{X}\right) \end{Bmatrix}, \tag{7}$$

where the subscripts '*m*' and '*u*' denote the measured and unmeasured regions, respectively. For a controlled test, the input is always measured, i.e. $\boldsymbol{P}_u = \mathbf{0}$. We will now perform a standard linear expansion before accounting for the nonlinear response data using high-amplitude testing.

2.2. Expansion of underlying linear response

As shown in Fig. 2, Step 1 of the expansion strategy is to apply linear experimental modal analysis followed by a mature linear expansion technique [12-14] (Step 2) for data using low-amplitude testing across the entire frequency range of interest. They are briefly outlined in the following for completeness.

2.2.1. Linear experimental modal analysis (Step 1)

The receptance matrix $\mathbf{H}$ of the underlying linear system (Eq. (5)) is partially measured at a limited set of DOFs and within the frequency range of interest during a test. The measured receptance function h_{ij} between response DOF *i* and reference DOF *j* can be described by modal parameters within this frequency range [22], as

$$h_{ij}\left(\omega\right) = \underbrace{\sum_{k=1}^{N_l-1}\left(\frac{r_{kij}}{\mathrm{j}\omega-\lambda_k}+\frac{r_{kij}^*}{\mathrm{j}\omega-\lambda_k^*}\right)}_{\text{lower residual}} + \sum_{k=N_l}^{N_l+N_k-1}\left(\frac{r_{kij}}{\mathrm{j}\omega-\lambda_k}+\frac{r_{kij}^*}{\mathrm{j}\omega-\lambda_k^*}\right) + \underbrace{\sum_{k=N_l+N_k}^{\infty}\left(\frac{r_{kij}}{\mathrm{j}\omega-\lambda_k}+\frac{r_{kij}^*}{\mathrm{j}\omega-\lambda_k^*}\right)}_{\text{upper residual}}, \tag{8}$$

where r_{kij} and λ_k denote the residue and pole values for mode *k*, respectively and $\bullet^*$ designates a complex conjugate. As depicted in Fig. 1, a total of N_k linear modes of the system are within the entire frequency range of interest; they are from mode N_l to mode ($N_l + N_k - 1$) and are captured by the middle summation term in Eq. (8). The other two terms – the lower residual and the upper residual – denote the out-of-band modal contributions. Note that the parameters r_{kij}, λ_k and N_k are obtained using the linear experimental modal analysis.

The linear experimental modal analysis begins with determining the model order N_k using measured FRFs, i.e. determining the number of modes in Eq. (8) to fit the measured FRF data. Here, we use the established stabilisation diagram [23], in which the FRFs are fitted with an increasing model order and the poles are plotted by different symbols according to the stability thresholds defined for natural frequency and damping ratio of a pole. The fitting method can

choose from the established least-squares complex exponential (LSCE) method [22,25,26] or the PolyMAX method [23,24]; both of which have been extensively used for analysing data of industrial structures in the presence of measurement noise [23]. Here we will demonstrate their compatibility with our proposed nonlinear expansion strategy with illustrative examples in Section 3 and Section 4.

Having determined the order of the model, the modal parameters can be extracted by fitting the FRFs to this specified model order as

$$h_{ij}(\omega) = \sum_{k=N_l}^{N_l+N_k-1}\left(\frac{r_{kij}}{\mathrm{j}\omega-\lambda_k}+\frac{r_{kij}^*}{\mathrm{j}\omega-\lambda_k^*}\right)-\frac{LR}{\omega^2}+UR, \tag{9}$$

where *LR* and *UR* denote the lower residual mass and upper residual stiffness. The fitting gives estimates of the residues r_{kij} and poles λ_k. Thereby, the modal parameters (natural frequency ω_{n_k}, modal damping ratio ξ_k, and mode shape ϕ_{ik}) for each mode *k* are estimated by

$$\lambda_k, \lambda_k^* = -\xi_k\omega_{r_k} \pm \mathrm{j}\omega_{r_k}\sqrt{1-\xi_k^2}, \tag{10}$$

$$\alpha_k\phi_{ik}\phi_{jk} = r_{kij}, \quad k = 1,2,\cdots N_k, \tag{11}$$

where the scaling constant $\alpha_k = \dfrac{1}{2\mathrm{j}m_{r_k}\omega_{r_k}}$. m_{r_k} denotes the modal mass for mode *k*, which is typically normalised to unity with measured driving-point FRFs [22].

The results of linear experimental analysis can now be summarised as

$$\boldsymbol{\Lambda}^{\text{Meas}} = \text{diag}\left[\omega_{nN_l}, \omega_{n(N_l+1)}, \cdots \omega_{nN_k}\right], \quad \boldsymbol{\Xi}^{\text{Meas}} = \text{diag}\left[\xi_{N_l}, \xi_{N_l}, \cdots \xi_{N_k}\right], \tag{12}$$

$$\boldsymbol{\Phi}_m^{\text{Meas}} = \begin{bmatrix} \phi_{i_1,N_l} & \phi_{i_1,(N_l+1)} & \cdots & \phi_{i_1,N_k} \\ \phi_{i_2,N_l} & \phi_{i_2,(N_l+1)} & & \phi_{i_2,N_k} \\ \vdots & & & \\ \phi_{i_{N_m},N_l} & \phi_{i_{N_m},(N_l+1)} & \cdots & \phi_{i_{N_m},N_k} \end{bmatrix}. \tag{13}$$

where $i_1, i_2, \cdots i_{N_m}$ denotes the measured DOFs with a total number of N_m. Note that the mass-normalised mode shapes $\boldsymbol{\Phi}_m^{\text{Meas}} \in \mathbb{R}^{N_m \times N_k}$ in Eq. (13) are only obtained at measured locations, i.e. they are spatially incomplete.

2.2.2. Linear FRF expansion (Step 2)

With the mode shapes estimated from the measured data, we now expand them to unmeasured DOFs. Recall that the modal damping ratios, $\boldsymbol{\Xi}^{\text{Meas}}$, and modal frequencies, $\boldsymbol{\Lambda}^{\text{Meas}}$, have already been estimated and are still the same for the responses at unmeasured DOFs, only the modal shapes require expansion.

Additionally, as pre-assumed in Section 2.1, a finite-element model for the underlying linear system is available. Therefore, the measured shapes can be expanded by the system equivalent reduction expansion process (SEREP) [12, 14], where the measured mode shapes are assumed to be a linear combination of the mode shapes from the finite-element analysis through a transformation matrix $\mathbf{T}$, i.e.,

$$\begin{Bmatrix} \boldsymbol{\Phi}_m^{\text{Meas}} \\ \boldsymbol{\Phi}_u \end{Bmatrix} = \begin{Bmatrix} \boldsymbol{\Phi}_m^{\text{FE}} \\ \boldsymbol{\Phi}_u^{\text{FE}} \end{Bmatrix} \mathbf{T}, \tag{14}$$

where $\boldsymbol{\Phi}_m^{\text{FE}} \in \mathbb{R}^{N_m \times N_k}$ and $\boldsymbol{\Phi}_u^{\text{FE}} \in \mathbb{R}^{N_u \times N_k}$ are mode shape matrices of the underlying linear system from the finite-element analysis in the measured and unmeasured regions, respectively. $\boldsymbol{\Phi}_m^{\text{Meas}} \in \mathbb{R}^{N_m \times N_k}$ are measured mode shapes (Eq. (13)). $\boldsymbol{\Phi}_u \in \mathbb{R}^{N_u \times N_k}$ includes mode shapes in the unmeasured region, which are required to be estimated. Note that only the modes that are well correlated between the finite-element analysis and measured data are included in the expansion [14].

A pseudo-inverse of the upper equation of Eq. (14) is used to obtain the transformation matrix $\mathbf{T} \in \mathbb{R}^{N_k \times N_k}$

$$\mathbf{T} = \left(\left(\boldsymbol{\Phi}_m^{\text{FE}} \right)^{\text{T}} \boldsymbol{\Phi}_m^{\text{FE}} \right)^{-1} \left(\boldsymbol{\Phi}_m^{\text{FE}} \right)^{\text{T}} \boldsymbol{\Phi}_m^{\text{Meas}}. \tag{15}$$

The unmeasured shapes can now be estimated using the lower equation of Eq. (14)

$$\hat{\boldsymbol{\Phi}}_u = \boldsymbol{\Phi}_u^{\text{FE}} \mathbf{T}, \tag{16}$$

where $\hat{\boldsymbol{\Phi}}_u$ denotes an estimate of $\boldsymbol{\Phi}_u$.

Substituting the estimated unmeasured mode shapes, $\hat{\boldsymbol{\Phi}}_u$, into Eq.(11), the unmeasured FRFs ($\hat{\mathbf{H}}_{mu}$, $\hat{\mathbf{H}}_{um}$ and $\hat{\mathbf{H}}_{uu}$) can now be expanded by Eq.(8), since other parameters - the poles, the lower residual mass and the upper residual stiffness - have already been identified using measured FRFs.

2.3 Expansion of nonlinear response

The technique for the expansion of nonlinear responses proposed here utilises the modal parameters identified from the measured linear FRF data and relies on additional unknown parameters introduced to describe the nonlinearities; the number of these unknown parameters should be kept as small as possible to avoid overfitting. To this end, the expansion technique is now divided into two separate categories according to different types of nonlinear structures: 1) structures with localised nonlinearities, such as nonlinear joints [3,10] or attachments [27]. It will be described in Step 3-L; 2) structures with distributed nonlinearities, for example, geometrically nonlinear beams [28,29] or plates [30-32]; the derivations are elaborated in Step 3-D as follows.

2.3.1. Structure with localised nonlinearities (Step 3-L)

For a structure with γ localised nonlinearities, the number of independent nonlinear elements is far fewer than the total DOFs of the structure. Therefore, the nonlinearities are described using physical coordinates.

Using an assumed, or pre-identified, location matrix, the dynamic equation of Eq. (7) can be written as [20]

$$\begin{Bmatrix} \boldsymbol{X}_m \\ \boldsymbol{X}_u \end{Bmatrix} = \begin{bmatrix} \mathbf{H}_{mm} & \mathbf{H}_{mu} \\ \mathbf{H}_{um} & \mathbf{H}_{uu} \end{bmatrix} \begin{Bmatrix} \boldsymbol{P}_m \\ \boldsymbol{P}_u \end{Bmatrix} - \begin{bmatrix} \mathbf{H}_{mm} & \mathbf{H}_{mu} \\ \mathbf{H}_{um} & \mathbf{H}_{uu} \end{bmatrix} \begin{bmatrix} \mathbf{L}_m \\ \mathbf{L}_u \end{bmatrix} \boldsymbol{F}_{\mathrm{nl}}, \tag{17}$$

where vector $\boldsymbol{F}_{\mathrm{nl}} \in \mathbb{C}^{\gamma \times 1}$ includes all non-zero terms in the nonlinear force vector $\boldsymbol{F} \in \mathbb{C}^{N \times 1}$ in Eq. (6). $\mathbf{L}_m \in \mathbb{R}^{N_m \times 1}$ and $\mathbf{L}_u \in \mathbb{R}^{N_u \times 1}$ denote the location matrices of nonlinear elements in the measured and unmeasured region, respectively. Note that DOFs connected to the nonlinear elements are generally associated with joints, contacting interfaces or connections of nonlinear devices. If unknown, they should be located before this step using a location method such as the one discussed in [19].

The relative motion of independent nonlinear elements, $\boldsymbol{R} \in \mathbb{C}^{\gamma \times 1}$, can be written as [20]

$$\boldsymbol{R} = \begin{bmatrix} \mathbf{L}_m^{\mathrm{T}} & \mathbf{L}_u^{\mathrm{T}} \end{bmatrix} \boldsymbol{X} \tag{18}$$

Note that the unmeasured underlying linear FRFs - $\mathbf{H}_{mu}$, $\mathbf{H}_{um}$ and $\mathbf{H}_{uu}$ in Eq. (7) - have already been obtained in the previous section through expansion, the output residual $\boldsymbol{\varepsilon}^{\mathrm{OR}} \in \mathbb{C}^{N_m \times 1}$ (the top of Eq. (17)) can thus be obtained as

$$\boldsymbol{\varepsilon}^{\mathrm{OR}} = \mathbf{H}_{mm}^{\mathrm{Meas}} \boldsymbol{P}_m - \left(\mathbf{H}_{mm}^{\mathrm{Meas}} \mathbf{L}_m + \hat{\mathbf{H}}_{mu} \mathbf{L}_u \right) \boldsymbol{F}_{\mathrm{nl}} - \boldsymbol{X}_m. \tag{19}$$

The nonlinear forces are estimated by finding the solution for

$$\hat{\boldsymbol{F}}_{\mathrm{nl}} = \arg\min_{\boldsymbol{F}_{\mathrm{nl}}} \left\| \boldsymbol{\varepsilon}^{\mathrm{OR}} \right\|^2 . \tag{20}$$

Note that Eq. (20) is over-determined if the number of measured channels is greater than the number of independent nonlinear elements. Next, the type of nonlinear elements is non-parametrically characterised using the Equivalent Dynamic Stiffness Mapping method [20,33], and so fitted to a model of the form

$$\hat{F}_{\mathrm{nl},i} \approx \left(\sum_{k=1}^{N_i^{\mathrm{real}}} \mathrm{g}_k^{\mathrm{real}}(\boldsymbol{\theta}) + \mathrm{j} \sum_{k=1}^{N_i^{\mathrm{imag}}} \mathrm{g}_k^{\mathrm{imag}}(\boldsymbol{\theta}) \right) R_i, \quad i = 1, 2, \cdots \gamma, \tag{21}$$

where $\mathrm{g}_k^{\mathrm{real}}$ and $\mathrm{g}_k^{\mathrm{imag}}$ denote the basis functions for the real and imaginary components of ith nonlinear element, respectively. N_i^{real} and N_i^{imag} denote the number of basis functions to fit the real and imaginary parts of ith nonlinear forces, respectively. $\boldsymbol{\theta}$ includes all the coefficients used to describe the nonlinearities. R_i denotes the relative motion of the ith nonlinear element (Eq. (18)). The coefficients can also be refined by substituting Eq. (21) and (19) into Eq. (20), giving

$$\hat{\boldsymbol{\theta}} = \arg\min_{\boldsymbol{\theta}} \left\| \boldsymbol{\varepsilon}^{\mathrm{OR}} \right\|^2 \tag{22}$$

where $\hat{\boldsymbol{\theta}}$ is an estimate of the nonlinear coefficients vector $\boldsymbol{\theta}$. A detailed description with illustrative examples of the nonlinear coefficients estimation process (Eqs. (20) to (22)) is documented in [20].

Once all the coefficients describing the nonlinear features are obtained for a localised structure, the responses at unmeasured DOFs can be expanded by solving Eq. (17) using measured input forcing levels $\boldsymbol{P}_m^{\mathrm{Meas}}$, such that

$$\begin{Bmatrix} \hat{\boldsymbol{X}}_m \\ \hat{\boldsymbol{X}}_u \end{Bmatrix} = \begin{bmatrix} \mathbf{H}_{mm}^{\mathrm{Meas}} & \hat{\mathbf{H}}_{mu} \\ \hat{\mathbf{H}}_{um} & \hat{\mathbf{H}}_{uu} \end{bmatrix} \begin{Bmatrix} \boldsymbol{P}_m^{\mathrm{Meas}} \\ \mathbf{0} \end{Bmatrix} - \begin{bmatrix} \mathbf{H}_{mm}^{\mathrm{Meas}} & \hat{\mathbf{H}}_{mu} \\ \hat{\mathbf{H}}_{um} & \hat{\mathbf{H}}_{uu} \end{bmatrix} \begin{bmatrix} \mathbf{L}_m \\ \mathbf{L}_u \end{bmatrix} \boldsymbol{F}_{\mathrm{nl}} \left(\hat{\boldsymbol{\theta}}, \hat{\boldsymbol{X}}_m, \hat{\boldsymbol{X}}_u \right). \tag{23}$$

The nonlinear responses at measured ($\hat{\boldsymbol{X}}_m$) and unmeasured DOFs ($\hat{\boldsymbol{X}}_u$) obtained by solving Eq. (23) are called *synthesised response* and *expanded response*, respectively, in this paper. One check that can be done is to compare the synthesised response $\hat{\boldsymbol{X}}_m$ to measured $\boldsymbol{X}_m^{\mathrm{Meas}}$ data to confirm the accuracy of the nonlinear expansion results. After that, Eq. (23) can also be solved at unmeasured input forcing levels; the computed response is then called *predicted response*.

2.3.2. Structure with distributed nonlinearities (Step 3-D)

For structures with distributed nonlinearities, it is beneficial to project the dynamic equation onto the linear modes to minimise the number of unknown parameters. Recall that we denote N_q modes that are affected by nonlinearities, as shown in Fig. 1, they are from mode N_{nl} to mode $\left(N_{nl}+N_q-1\right)$. Denoting a transformation into linear modal coordinates as

$$\begin{Bmatrix} \boldsymbol{x}_m \\ \boldsymbol{x}_u \end{Bmatrix} = \begin{Bmatrix} \boldsymbol{\Phi}_m^{\text{Meas}} \\ \hat{\boldsymbol{\Phi}}_u \end{Bmatrix} \boldsymbol{q}, \tag{24}$$

where $\boldsymbol{\Phi}_m^{\text{Meas}}$ and $\hat{\boldsymbol{\Phi}}_u$ are the measured mode shapes and the expanded mode shapes using low-amplitude testing in the previous section, respectively. Vector $\boldsymbol{q} \in \mathbb{R}^{N_q \times 1}$ denotes linear modal coordinates.

The dynamic equation, Eq. (1), can now be expressed by modal coordinates in the frequency domain. Consider mode *k* in the nonlinear frequency band (Fig. 1), we have

$$\left(-\omega^2 + 2\mathrm{j}\xi_k\omega_{r_k}\omega + \omega_{r_k}^2\right)Q_k + F_{r_k} = P_{r_k}, \quad k = N_{nl}, \left(N_{nl}+1\right), \cdots \left(N_{nl}+N_q-1\right), \tag{25}$$

while m_r=1 for a mass-normalised mode shape. ξ_k and ω_{r_k} are estimated from low-amplitude testing, as shown in Eq. (12), $P_{r_k} = \boldsymbol{\phi}_k^{\mathrm{T}}\boldsymbol{P}$, Q_k denotes the primary harmonic term of the modal response q_k, and F_{r_k} is an unknown modal nonlinear force. For a geometrically nonlinear structure these forces are usually adequately fitted using a series of polynomial functions of relevant modal coordinates [28,29,32], i.e. the basis functions can be chosen as

$$F_{r_k} \approx \sum_{i=1}^{N_{poly,k}^{\text{real}}} g_i^{\text{real}}\left(\boldsymbol{\theta},\boldsymbol{Q}\right) + \sum_{i=1}^{N_{poly,k}^{\text{imag}}} g_i^{\text{imag}}\left(\boldsymbol{\theta},\boldsymbol{Q}\right), \quad k = N_{nl}, \left(N_{nl}+1\right), \cdots \left(N_{nl}+N_q-1\right), \tag{26}$$

where $N_{poly,k}^{\text{real}}$ and $N_{poly,k}^{\text{imag}}$ are the number of basis functions used to fit the real and imaginary part of the *k*th modal nonlinear force, respectively. $\boldsymbol{\theta}$ contains all the nonlinear coefficients. The modal responses $\boldsymbol{Q} \in \mathbb{C}^{N_q \times 1}$ can be estimated by taking the pseudo-inverse of the upper equation of Eq. (24),

$$\hat{\boldsymbol{Q}} = \left(\left(\boldsymbol{\Phi}_m^{\text{Meas}}\right)^{\mathrm{T}}\boldsymbol{\Phi}_m^{\text{Meas}}\right)^{-1}\left(\boldsymbol{\Phi}_m^{\text{Meas}}\right)^{\mathrm{T}}\boldsymbol{X}_m^{\text{Meas}}, \tag{27}$$

where $\hat{\boldsymbol{Q}}$ denotes an estimate of $\boldsymbol{Q}$.

The *k*th modal equation residual, $\varepsilon_k^{\mathrm{MER}}$, can thus be written as

$$\varepsilon_k^{\mathrm{MER}} = P_{r_k} - \left(-\omega^2 + 2\mathrm{j}\xi_k\omega_{r_k}\omega + \omega_{r_k}^2\right)\hat{Q}_k - F_{r_k}, \quad k = N_{nl}, \left(N_{nl}+1\right), \cdots \left(N_{nl}+N_q-1\right). \tag{28}$$

Grouping the residuals into a vector $\boldsymbol{\varepsilon}^{\mathrm{MER}} = \left[\varepsilon_{N_{nl}}^{\mathrm{MER}}, \varepsilon_{N_{nl}+1}^{\mathrm{MER}}, \mathrm{L}\ \varepsilon_{\left(N_{nl}+N_q-1\right)}^{\mathrm{MER}}\right]$, the nonlinear coefficients are estimated by finding the solution for

$$\hat{\boldsymbol{\theta}} = \arg\min_{\boldsymbol{\theta}} \left\| \boldsymbol{\varepsilon}^{\mathrm{MER}} \right\|^2, \tag{29}$$

where $\hat{\boldsymbol{\theta}}$ denotes an estimate of $\boldsymbol{\theta}$.

Finally, by substituting the estimated $\hat{\boldsymbol{\theta}}$ into Eq. (25), the nonlinear modal dynamic equation can be solved and the modal responses, $\hat{\boldsymbol{Q}}$, can be obtained. Using Eq. (24), the responses can be obtained

$$\begin{Bmatrix} \hat{\boldsymbol{X}}_m \\ \hat{\boldsymbol{X}}_u \end{Bmatrix} = \begin{Bmatrix} \boldsymbol{\Phi}_m^{\mathrm{Meas}} \\ \hat{\boldsymbol{\Phi}}_u \end{Bmatrix} \hat{\boldsymbol{Q}}. \tag{30}$$

Similarly, the nonlinear responses in the measured region ($\hat{\boldsymbol{X}}_m$) and unmeasured region ($\hat{\boldsymbol{X}}_u$) are called *synthesised response* and *expanded response*, respectively. A check between the synthesised responses, $\hat{\boldsymbol{X}}_m$, and the measured data, $\boldsymbol{X}_m^{\mathrm{Meas}}$, can confirm the accuracy of the expansion process. The nonlinear dynamic equation is then solved at unmeasured input forcing levels and the obtained response is called *predicted response* in this paper.

2.4. Summary of the expansion strategy

The proposed nonlinear expansion strategy follows the same philosophy of linear expansion technique: relying on experimental modal analysis of the measured data and involving the finite-element model only as much as necessary to fill in the missing information. In this strategy, the modal properties of the underlying linear system are extracted from measured low-amplitude data using linear modal analysis; the nonlinear coefficients are then estimated using the residuals of responses between low-amplitude and high-amplitude testing. The finite-element model is only used for expansion of mode shapes of the underlying linear system. A comparison of linear and nonlinear expansion techniques is listed in Table 2.

Table 2

Comparison of linear and nonlinear expansion techniques

	Measured linear part	Unmeasured linear part	Basis function of nonlinear part
Linear expansion technique [12-14]	Modal model	Mode shape expansion using finite-element model	N/A
Nonlinear expansion technique	Modal model (Step 1)	Mode shape expansion using finite-element model (Step 2)	Physical coordinates for localised nonlinearities (Step 3-L)
			Modal coordinates for distributed nonlinearities (Step 3-D)

3. Example with localised nonlinearity

3.1. Numerical model

A numerical example of a two-beam system connected by a nonlinear spring is considered in this section. Two models of the system are built to demonstrate the expansion technique: the first is a simulated 'experimental model' – used to generate simulated data with noise added to the outputs. The second is a finite-element model of the underlying linear system. In engineering practice, the discrepancies between the finite-element model and the measured data are minimised by adjusting the parameters in the model; however, errors still exist due to uncertainties and measurement noise even after the linear model is updated. To simulate these post-updating inaccuracies, the parameters of the finite-element model considered here are deliberately detuned. Detailed descriptions of the two models are now given.

3.1.1. Simulated experimental model

Fig. 3 shows a schematic of the model, where the system is modelled as two 7-node planar beams with a thickness of 1 mm, a width of 30mm, a Young's modulus of 210 GPa and a density of 7850 kg/m^3 for each element. A nonlinear spring is connected between DOFs 13 and 15. The lengths of the cantilever beams are slightly different, l_1=39 cm and l_2=40 cm. The linear stiffness of the connecting spring is 10 N/m. Proportional damping is assumed for the entire underlying linear system as

$$\mathbf{C} = \alpha\mathbf{M} + \beta\mathbf{K}, \quad \text{with:} \quad \alpha=0.5 \quad \text{and} \quad \beta=2\times10^{-5}. \tag{31}$$

The nonlinear part of the spring is

$$f_{\mathrm{nl}} = k_{\mathrm{nl}} r^3 + c_{\mathrm{nl}} \dot{r}^3, \quad \text{with:} \quad k_{\mathrm{nl}} = 5\times 10^3 \ \mathrm{N/m^3}, c_{\mathrm{nl}} = 70 \ \mathrm{N/(m/s)^3}. \tag{32}$$

Measurements are taken at six points (DOFs 3, 7, 11, 17, 21, 25), as indicated in Fig. 3 using blue dots. An input force is applied at both DOFs 7 and 21 with the same amplitude but opposite direction.

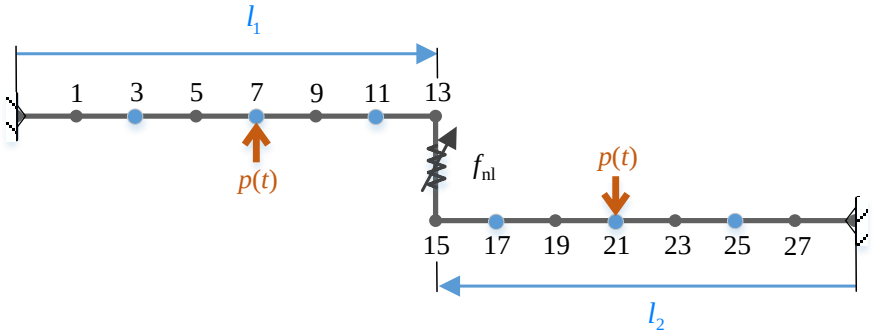

Fig. 3. Two cantilever beams connected by a nonlinear spring, where blue dots denote measured points.

The low-amplitude simulated data cover the first four modes of the system from 0.01 Hz to 45 Hz with a frequency resolution of 0.01 Hz where the force amplitude is given as 0.01 N; white noise with a standard deviation of 5×10^{-5} m is added to the measurements. The high-amplitude data are obtained using multiple levels of input force (0.1 N, 0.5 N and 1N), focused around the first two modes from 0.5 Hz to 25 Hz with a frequency resolution of 0.1 Hz. The measured data are simulated by considering a sinusoidal input force and integrating the dynamic equation using Runge-Kutta algorithm in MATLAB with a fixed time-step dividing each drive cycle into 300 equal steps; the primary harmonic terms of the data are then obtained using a fast Fourier transformation.

3.1.2. Updated finite-element model

A finite-element model, regarded as the updated finite-element model, of this system is used to model the underlying linear system shown in Fig. 3, i.e., neglecting the nonlinear component of the connecting spring. Note that the connecting spring has a linear stiffness, which is included in the finite-element model. In engineering practice, the discrepancies in natural frequencies between the test data and the finite-element model of a large-scale structure may be 5% after (linear) modal updating [34]. To reflect these modelling errors, the Young's modulus of both beams in the finite-element model was set to 190 GPa, representing a 9.52% error compared to the simulated experimental model. As

listed in Table 3, it introduces up to around 5% discrepancies of the first four natural frequencies between the two models.

Table 3

Frequencies of the underlying linear system of the simulated experimental model and the updated finite-element model.

Mode order	Natural frequency (Hz)		Difference in frequency (%)	Modal damping ratio (%)	
	Simulated experimental model	Updated finite-element model		Simulated experimental model	Updated finite-element model
1	5.3484	5.0882	4.87	0.7775	0.8140
2	7.0795	6.8784	2.84	0.6065	0.6217
3	32.8806	31.2892	4.84	0.3276	0.3238
4	34.6076	32.9381	4.82	0.3324	0.3278

3.2. Linear experimental modal analysis (Step 1)

The frequency range considered is from 0 to 20Hz, which covers the first two modes according to the (updated) finite-element model. Therefore, a linear modal testing up to 45 Hz is performed. The low-amplitude data are used for linear modal analysis to determine its order and modal parameters. As shown by the stabilisation diagram using the LSCE method [26] in Fig. 4, the averaged response functions are fitted with an increasing modal order, where the stability thresholds are 1% for the natural frequency and 5% for the damping ratio.

The modal parameters are identified using a model order of 5 and the first 4 modal parameters are extracted. The estimated natural frequencies and damping ratios are listed in Table 4.

We now use the identified modal properties to synthesise the data at the measured DOFs. A comparison of the simulated measured data, synthesised FRFs, and FRFs calculated from the finite-element model is shown at two representative locations in Fig. 5. It is demonstrated that the synthesised FRFs can better describe the dynamics near resonances than those directly computed from the finite-element model, which contains modelling errors in Young's modulus. This is often the case since the modal parameters used for synthesis are identified from measured data and hence do not suffer from modelling errors common in the (updated) finite-element models.

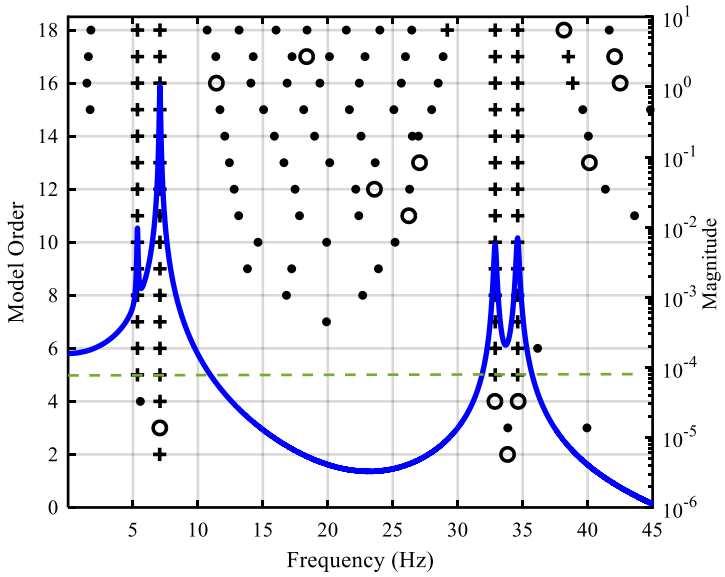

Fig. 4. Stabilisation diagram of the two-beam example. The blue curve (—) shows the averaged FRFs from 6 measured channels. A cross (+) denotes stabilisation in natural frequency and damping ratio; a circle (O) denotes stabilisation in natural frequency; a dot (•) denotes no stabilisation in natural frequency. The stabilisation thresholds for natural frequency, damping ratio are 1% and 5%, respectively. The green dashed line indicates the chosen model order.

The Modal Assurance Criterion (MAC) values of the identified mode shapes and the finite-element model are shown in Eq. (33). The diagonal dominance of the MAC values indicates that the identified modes and the modes computed from the finite-element model are well correlated.

$$\mathrm{MAC}=\begin{bmatrix} 0.9966 & 0.0024 & 0.0060 & 0.0025 \\ 0.0003 & 1.0000 & 0.0023 & 0.0052 \\ 0.0055 & 0.0022 & 0.9998 & 0.0001 \\ 0.0030 & 0.0049 & 0.0002 & 0.9999 \end{bmatrix} \tag{33}$$

Table 4

Identified natural frequencies and damping ratios of the first four modes.

Mode	Natural frequency (Hz)	Damping ratio (%)
1	5.3396	0.7800
2	7.0712	0.6057
3	32.8777	0.3312
4	34.6039	0.3292

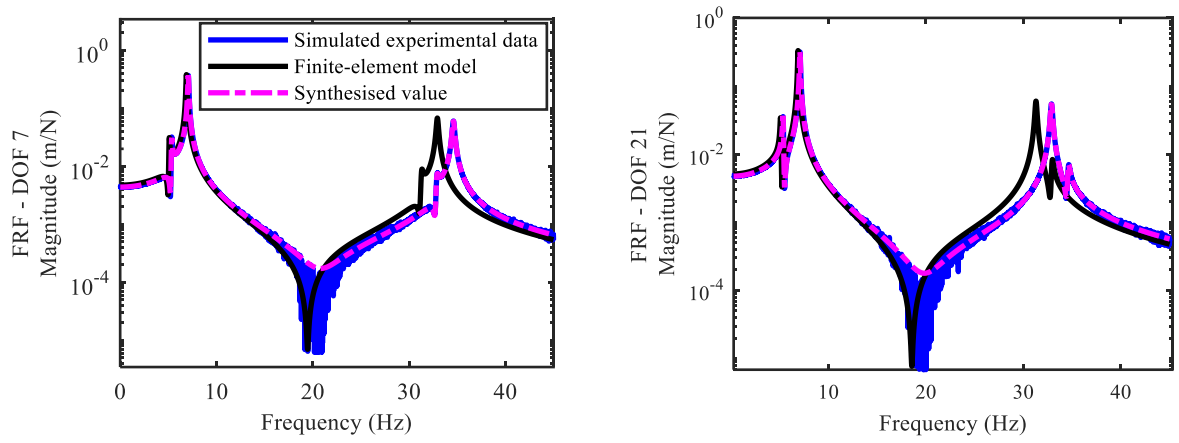

(a) (b)

Fig. 5. Comparison of FRFs obtained by measurement, finite-element model and synthesised values using identified modal parameters at two representative measured locations: (a) DOF 7 and (b) DOF 21.

3.3. Linear FRF expansion (Step 2)

The identified mode shapes are spatially incomplete, we now perform the expansion of the first four mode shapes using Eq. (16), where the transformation matrix $\mathbf{T}$ is obtained using Eq. (15) as

$$\mathbf{T}=\begin{bmatrix} 1.0016 & 0.0065 & 0.0002 & 0.0002 \\ -0.0504 & 0.9996 & 0.0029 & 0.0025 \\ 0.0000 & 0.0013 & 0.9998 & 0.0111 \\ -0.0002 & 0.0014 & -0.0126 & 0.9999 \end{bmatrix}. \tag{34}$$

Fig. 6 depicts the expanded unmeasured mode shapes. This clearly shows that the expansion provides a smoothed interpolation of the measured mode shapes.

A comparison between the simulated experimental data and expanded FRF using identified modal parameters at two points (DOF 13 and 15) that were not used in the identification process are shown in Fig. 7; it can be seen that they agree very well.

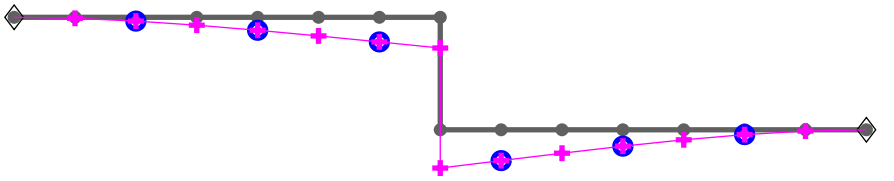

(a)

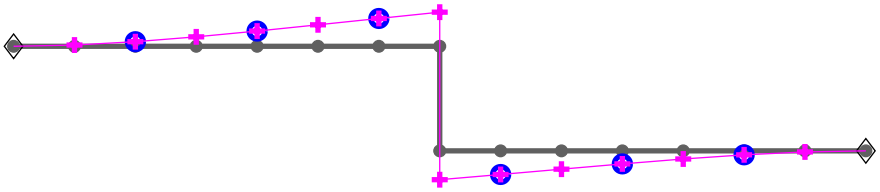

(b)

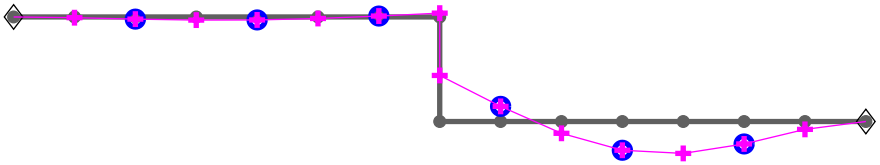

(c)

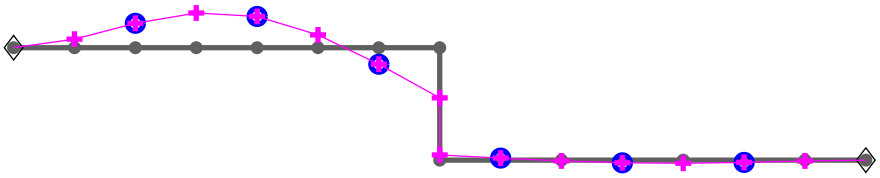

(d)

Fig. 6. Mode shape expansion of the first four linear modes: (a) first mode, (b) second mode, (c) third mode and (d) fourth mode, where grey lines denote the undeformed mode shape, blue circles denote the measured DOFs and pink crosses denote expanded mode shapes.

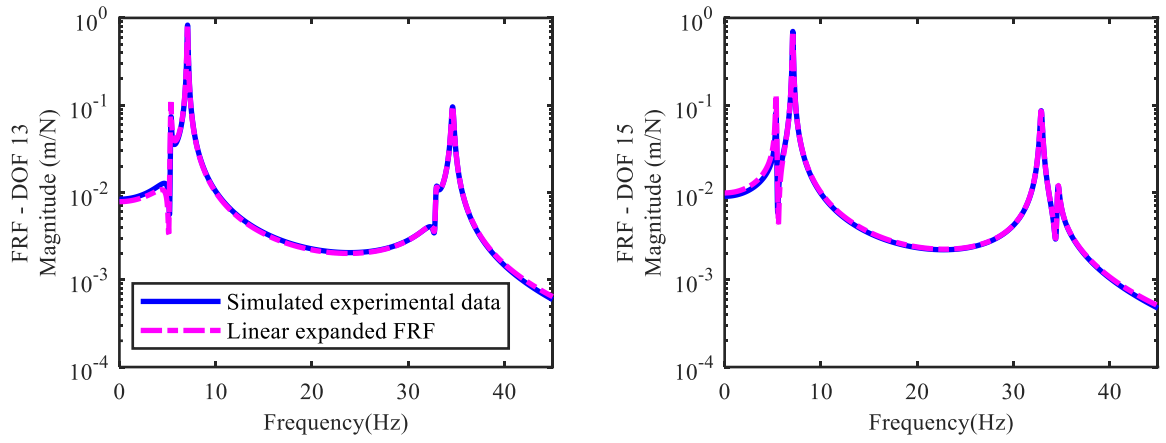

(a) (b)

Fig. 7. Comparison of FRFs computed using the simulated experimental model and expansion using identified modal parameters at two representative 'unmeasured' DOFs: (a) DOF 13 and (b) DOF 15.

3.4. Nonlinear response expansion (Step 3-L)

In this subsection, the measured nonlinear responses are now expanded to the unmeasured region building on the extracted linear modal properties. As described in subsection 3.1.1, the system is now driven by high-amplitude stepped-sine excitations of 0.2 N, 0.4 N, 0.8 N and 1.0 N. Fig. 8 depicts the measured nonlinear responses of two representative DOFs (DOFs 3 and 25). It can be seen that the second mode is highly affected by the nonlinearity and the resonance leans towards higher frequency with the increase of input force levels.

We assume that the unknown nonlinear element is located between DOFs 13 and 15, neither of which are directly measured as shown in Fig. 3. The nonlinear force and relative motion of this element can be extracted using Eq. (20) and Eq. (18), and the results are depicted in Fig. 9. Note that if the locations of the nonlinear elements are not assumed, a localisation algorithm [19] can be implemented before this step.

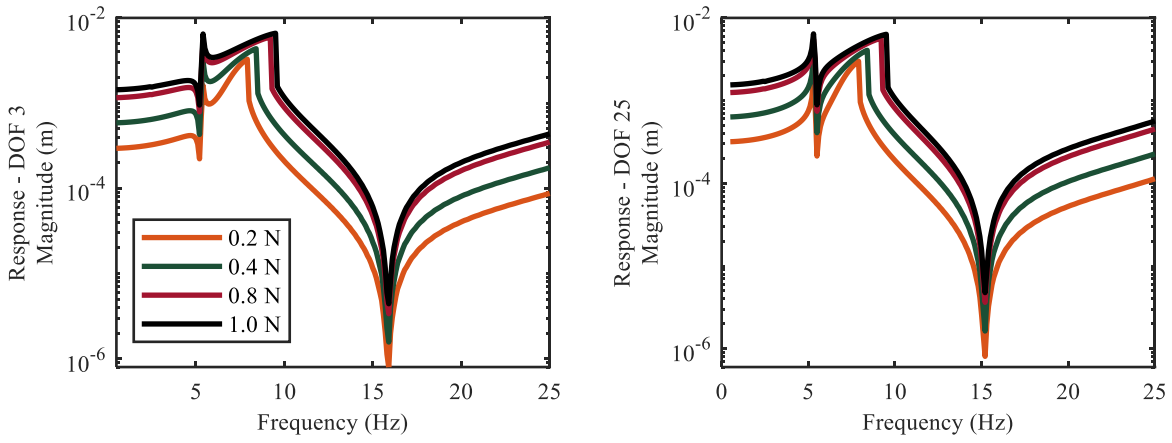

(a) (b)

Fig. 8. Measured responses at two representative DOFs with four input levels (0.2 N, 0.4 N, 0.8 N and 1.0 N): (a) DOF 3 and (b) DOF 25.

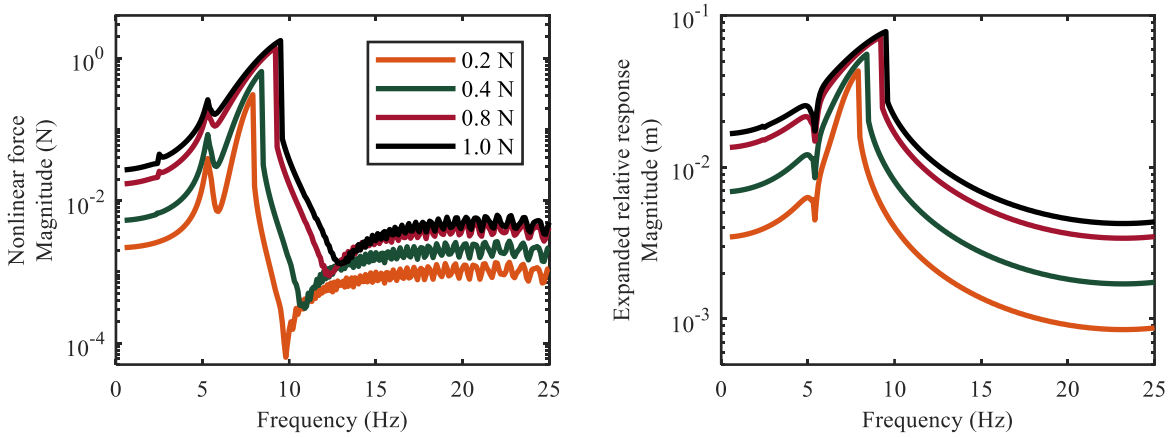

(a) (b)

Fig. 9. (a) Nonlinear force and (b) nonlinear relative motion extracted between DOFs 13 and 15 with four input levels (0.2 N, 0.4 N, 0.8 N and 1.0 N).

In order to obtain the nonlinear coefficients of the nonlinear spring, the Equivalent Dynamic Stiffness Mapping technique [20,33] is performed using the data in the frequency range from 5.8 Hz to 11.6 Hz, where nonlinear distortions are evident. The dynamic stiffness plot is shown in Fig. 10, where a quadratic term ($\bar{R}^2$) and a cubic term ($\omega\bar{R}^2$) are used as the basis functions to fit the stiffness and damping, respectively [33]. It gives estimates of the nonlinear coefficients as $\hat{k}_{\text{nl}} = 4.91\times10^3\ \text{N/m}^3$ (with 1.8% error) and $\hat{c}_{\text{nl}} = 66.13\,\text{N/(m/s)}^3$ (with 5.5% error), which achieves reasonable accuracy compared to their true values (Eq. (32)) in the simulated experimental model.

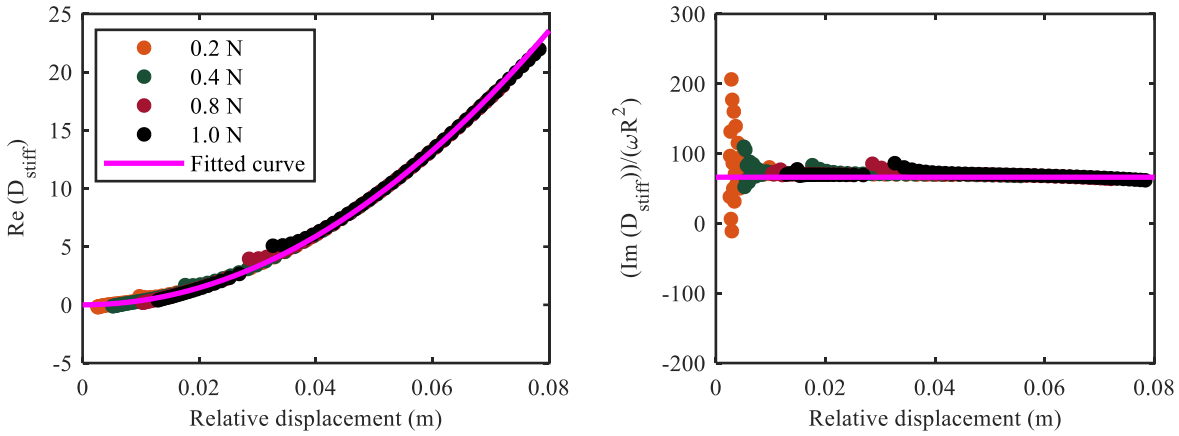

(a) (b)

Fig. 10. Equivalent Dynamic Stiffness plot of the nonlinear spring; (a) real and (b) imaginary components of the Equivalent Dynamic Stiffness against the amplitude of the relative displacement.

Substituting these identified nonlinear coefficients into the dynamic equation denoted by Eq. (23) and solving the equation using the measured input forcing levels, the synthesised responses are obtained. They are compared to the data that were used to identify the nonlinear coefficients in Fig. 11 at two representative DOFs (DOFs 7 and 21), which confirms that the systhesised response calculated using the identified nonlinear coefficients are in good agreement with the measured data.

Once the accuracy of the identified nonlinear coefficients is validated, the responses of the unmeasured DOFs can be expanded by solving Eq. (23). Fig. 12 depicts a comparison between the expanded responses calculated using the identified nonlinear coefficients and measured data at two DOFs (DOFs 13 and 15) that were not used in the identification. This shows that the expanded responses agree with the simulated measurement data very well.

The expansion technique is finally investigated by demonstrating its capability in predicting responses at unmeasured input forcing levels. Here a 0.6 N input level is used and the comparison is shown in Fig. 13. It can be clearly seen that the predicted response agrees very well with the data. Note that the 0.6 N input data were not used in the expansion; they are reserved only for validation.

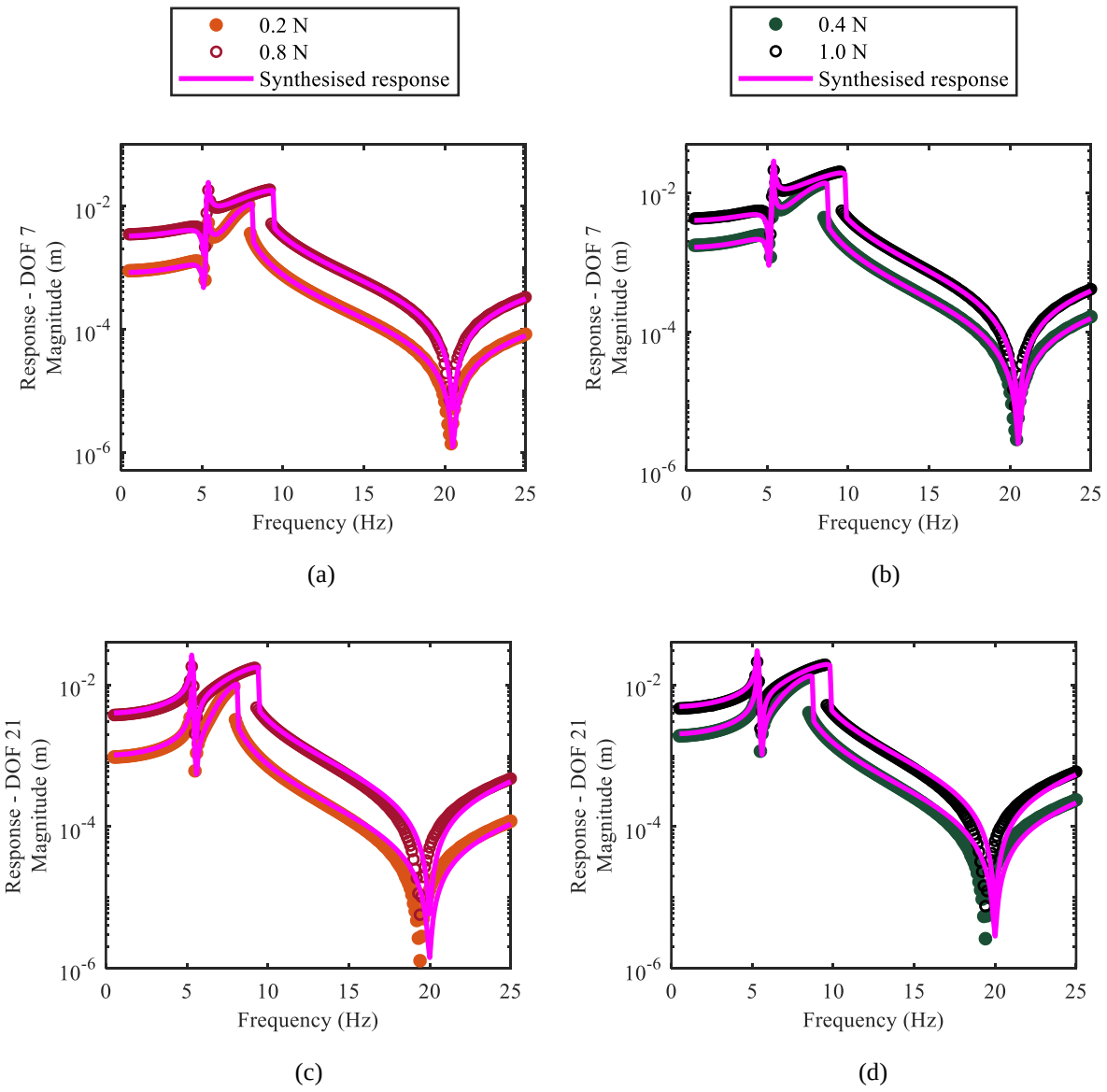

Fig. 11. Comparison between measured nonlinear response data and synthesised responses using identified nonlinear coefficients, where (a) and (b) show responses of DOF 7; (c) and (d) depict responses of DOF 21.

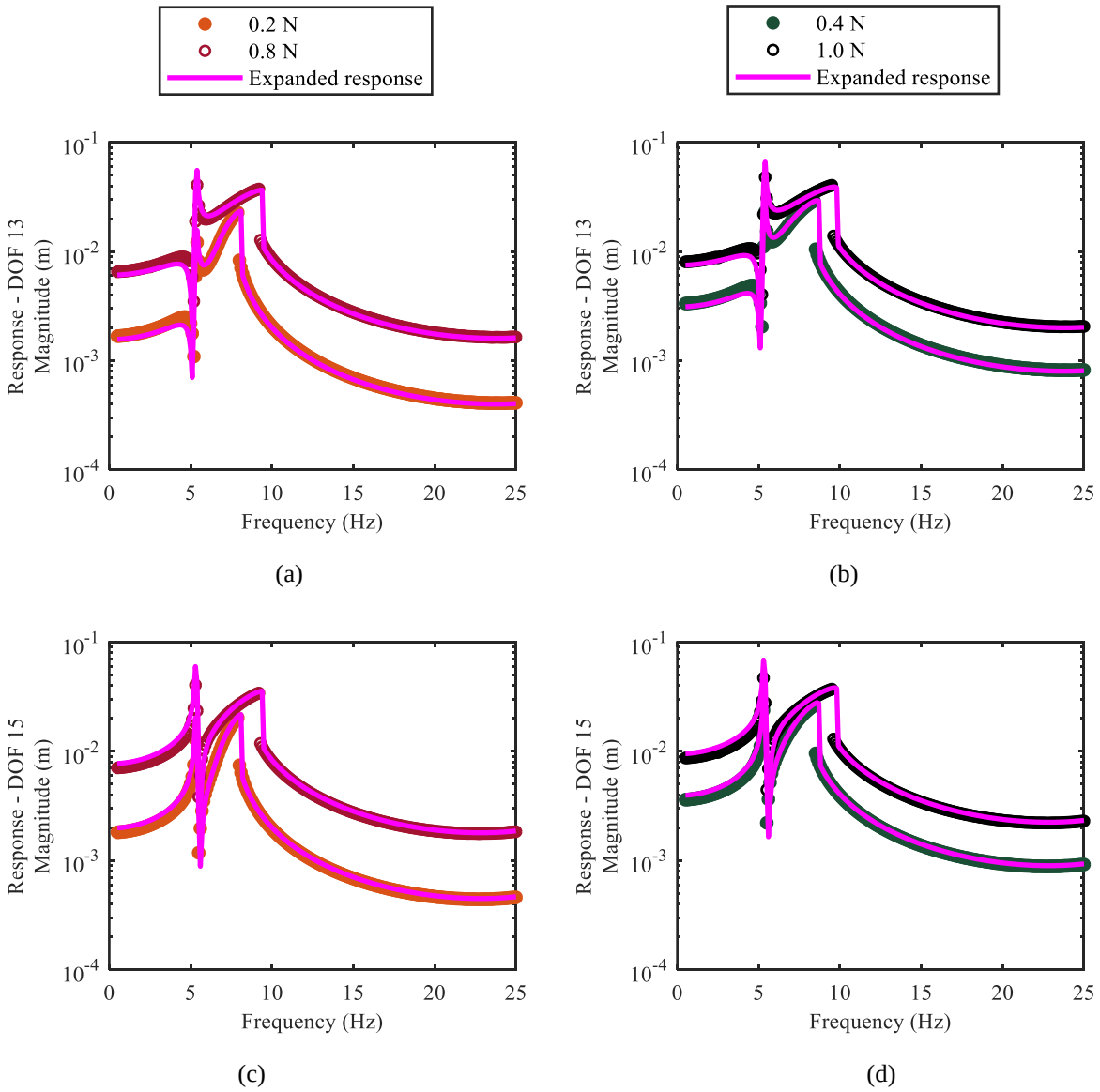

Fig. 12. Comparison between measured nonlinear response data and expanded responses using identified nonlinear coefficients, where (a) and (b) show responses of DOF 13; (c) and (d) depict responses of DOF 15.

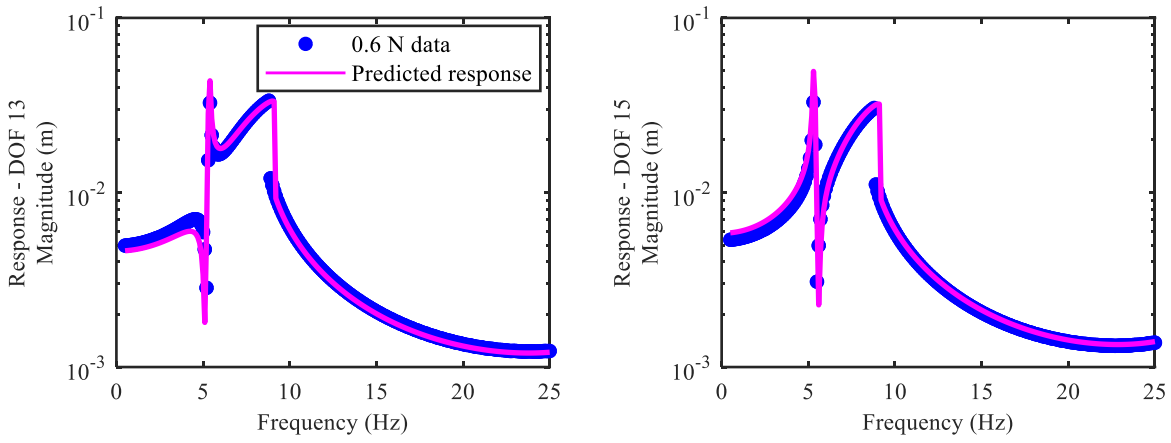

Fig. 13. Comparison between measured nonlinear response data and predicted responses using identified nonlinear coefficients at: (a) DOF 13 and (b) DOF 15 using a 0.6 N input force.

4. Experimental application to an asymmetric diesis-like structure

4.1. The physical structure

To demonstrate the proposed expansion technique further, we now apply it to experimental data of a diesis-like structure [28,35] depicted in Fig. 14. The structure consists of three steel beams: a main beam clamped at both ends, a cross-beam, with two concentrated masses, joined midspan-to-midspan with the main beam and a third smaller beam near one end of the main beam. The concentrated masses are adjustable allowing the natural frequency of the torsional mode to be detuned, as well as introducing asymmetry to the system. With this, the structure is adjusted to exhibit close linear natural frequencies between the fundamental bending and torsional modes. Nonlinear behaviour arises due to axial stretching of the main beam when it is vibrating at large response amplitudes.

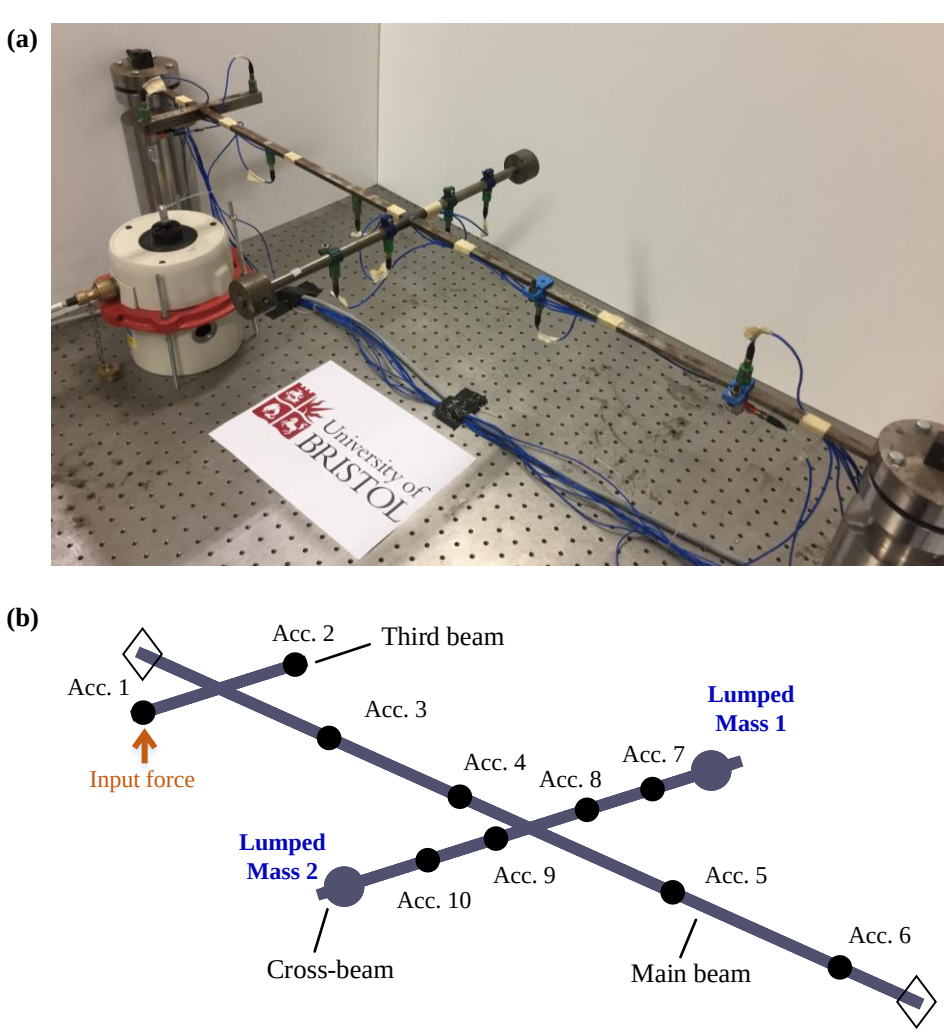

Fig. 14. Clamped-clamped diesis-like structure: (a) physical structure and (b) finite-element model with 1050 DOFs.

The dimensions of the structure are listed in Table 5. The two concentrated 218g masses are placed at a nominal distance of 195 mm and 199mm from the central line of the main beam, respectively. A finite element model of the structure is constructed with 173 beam elements and 12 lumped masses, where each of the accelerometers is 11g. In practice, the two masses are not exactly symmetrical and their mass centres are difficult to access, thereby their distances in the model will be slightly adjusted according to the measured dynamic data. As shown in Fig. 14(a), the structure is driven by a single shaker mounted on one end of the third beam allowing it to put sufficient energy into both modes. Data from eight accelerometers (Acc. 1, 2, 3, 5, 6, 7, 9, 10) are used for the expansion, the other two

accelerometers (Acc. 4 located on the main beam and Acc. 8 on the cross-beam) are reserved for validation of the expanded results.

Table 5

Dimensions of the beams

	Cross-section	Parameters
Main beam	Rectangular	Length:1010 mm; width: 12.7 mm; height: 6.3 mm
Cross-beam	Circular	Length: 448 mm; diameter: 12 mm
Third beam	Rectangular	Length: 178 mm; width: 15.8 mm; height: 15.8 mm

4.2. Linear experimental modal analysis (Step 1)

Our goal is to investigate the dynamics of the first two modes of this diesis-like structure; they are estimated to be around 16 Hz according to linear modal analysis of an initial finite-element model. During the test, we first apply a low-amplitude excitation to the structure to investigate its dynamics over a broad frequency range (5-95 Hz) with a frequency resolution of 0.1 Hz. Fig. 15(a) depicts the amplitudes of the measured FRFs using 0.01 N input. Two very closely-spaced modes are observed around 14 Hz, while the natural frequency of the third mode present in the measurement (near 69 Hz) is significantly higher than the first two modes. Therefore, we re-run the test and narrow the excitation frequency range down to a smaller frequency bandwidth (14-17 Hz) and a higher frequency resolution (0.01 Hz), as shown in Fig. 15(b).

The linear modal properties are identified using the data from the narrow frequency range (14-17 Hz) and low-amplitude input (0.01 N) using a standard linear experimental modal identification process. Fig. 16 depicts the stabilisation diagram used to determine the model order by fitting the eight measured FRF curves with increasing model orders using PolyMAX [23,24]. It can be seen that two vibrational modes meet the stability thresholds of both natural frequency and damping ratio; their natural frequencies and damping ratios are then estimated, see Table 6.

Synthesis of FRFs using the experimentally-extracted modal parameters is shown in Fig. 17 and compared to measured data at four representative channels. It can be seen that they agree well around resonances.

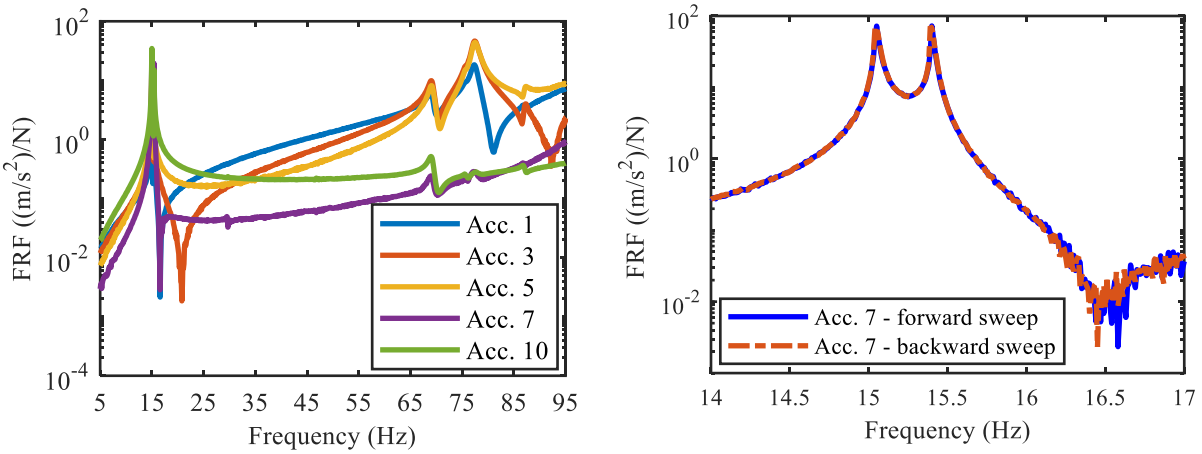

(a) (b)

Fig. 15. Measured FRFs at representative channels using 0.01 N input force: (a) broad frequency range; (b) close-up around the first two resonances with higher frequency resolution.

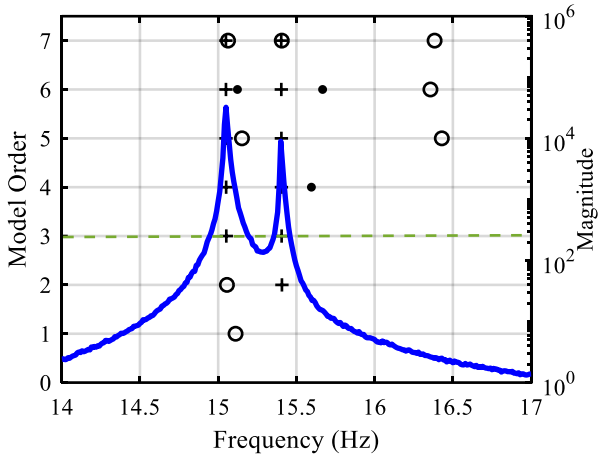

Fig. 16. Stabilisation diagram computed using data from narrow frequency range (14-17 Hz) and low-amplitude input (0.01 N). The blue curve (—) shows the averaged FRFs from eight measured channels. A cross (+) denotes stabilisation in natural frequency and damping ratio; a circle (○) denotes stabilisation in natural frequency; a dot (•) denotes no stabilisation in natural frequency. The stabilisation thresholds for natural frequency, damping ratio are 1% and 5%, respectively. The green dashed line indicates the chosen model order.

Table 6

First two modes of the diesis-like structure

Modal order	Modal frequencies (Hz)	Modal damping (%)
1	15.05	0.076
2	15.40	0.054

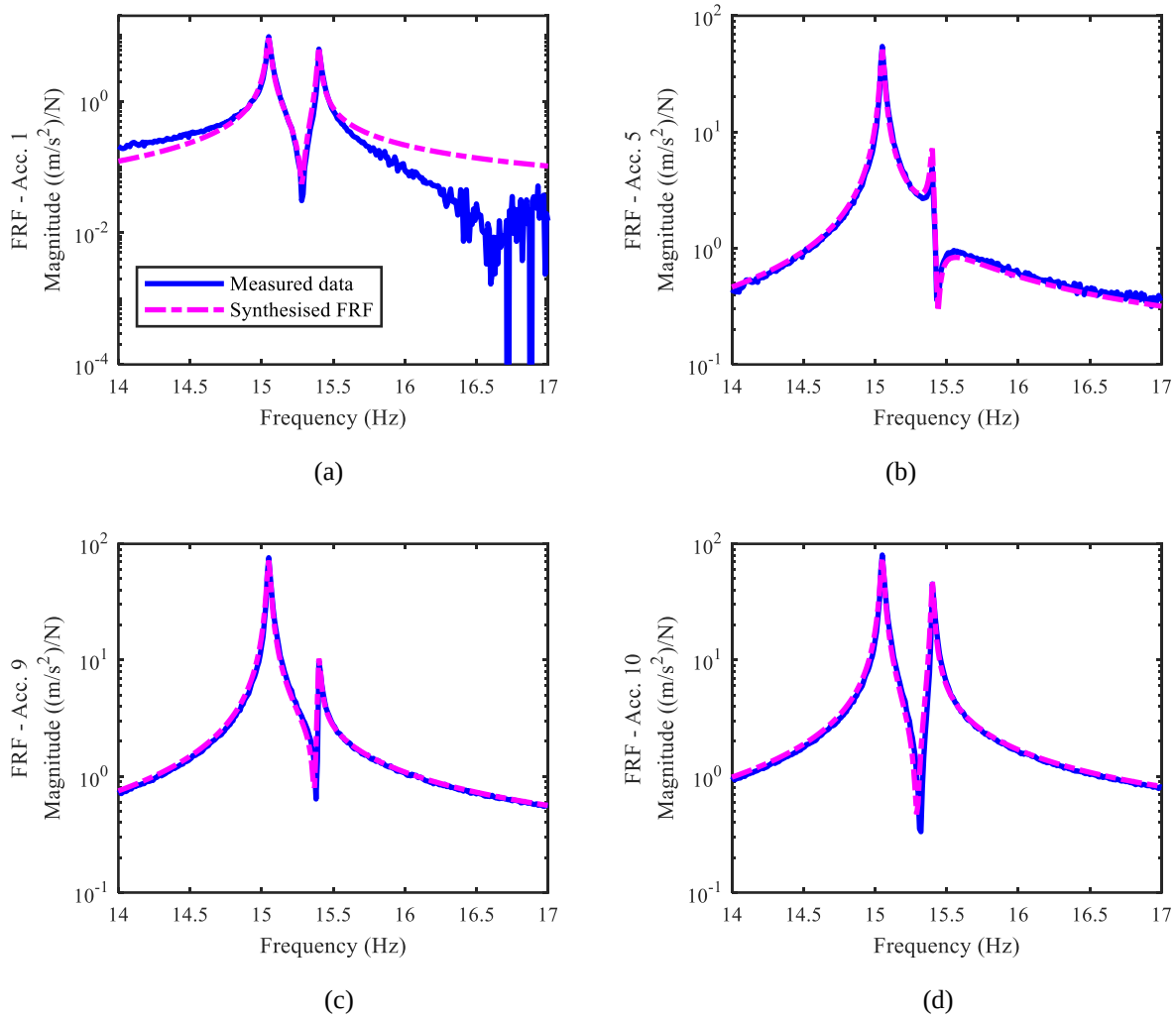

Fig. 17. Comparison of measured data and synthesised FRFs using experimentally-extracted modal properties at: (a) Acc. 1 (driving point), (b) Acc. 5 (on the main beam), (c) Acc. 9 (on the inside of the cross-beam) and (d) Acc. 10 (on the outside of the cross-beam).

4.3. Linear model updating and FRF expansion (Step 2)

With the experimentally-extracted modal properties, the initial finite-element model of the structure shown in Fig. 14 is now updated using the well-established linear finite-element model updating theory [14]: the distances of the concentrated lumped masses (Lumped Mass 1 and 2 shown in Fig. 14) are slightly adjusted in the model and a penalty function of mode shape discrepancies is minimised. The details are not discussed here; interested readers are directed to [14]. After several iterations, the distance of the Lumped Mass 1 converged to 194.5 mm and Lumped Mass 2 to 200.9 mm. The natural frequencies of the updated finite-element model are 15.02 Hz for the bending mode and 15.42 Hz for

the torsional mode, which are in good agreement with the measured values. Fig. 18(a)(b) depict the mode shapes from experimental modal analysis and Fig. 18(c)(d) depict the analytical mode shapes of the updated linear finite-element model. A comparison between the mode shapes of the measured data and the updated finite-element model using MAC values are given in Eq. (35), where the diagonal dominance of MAC values indicates good pairing of the mode shapes.

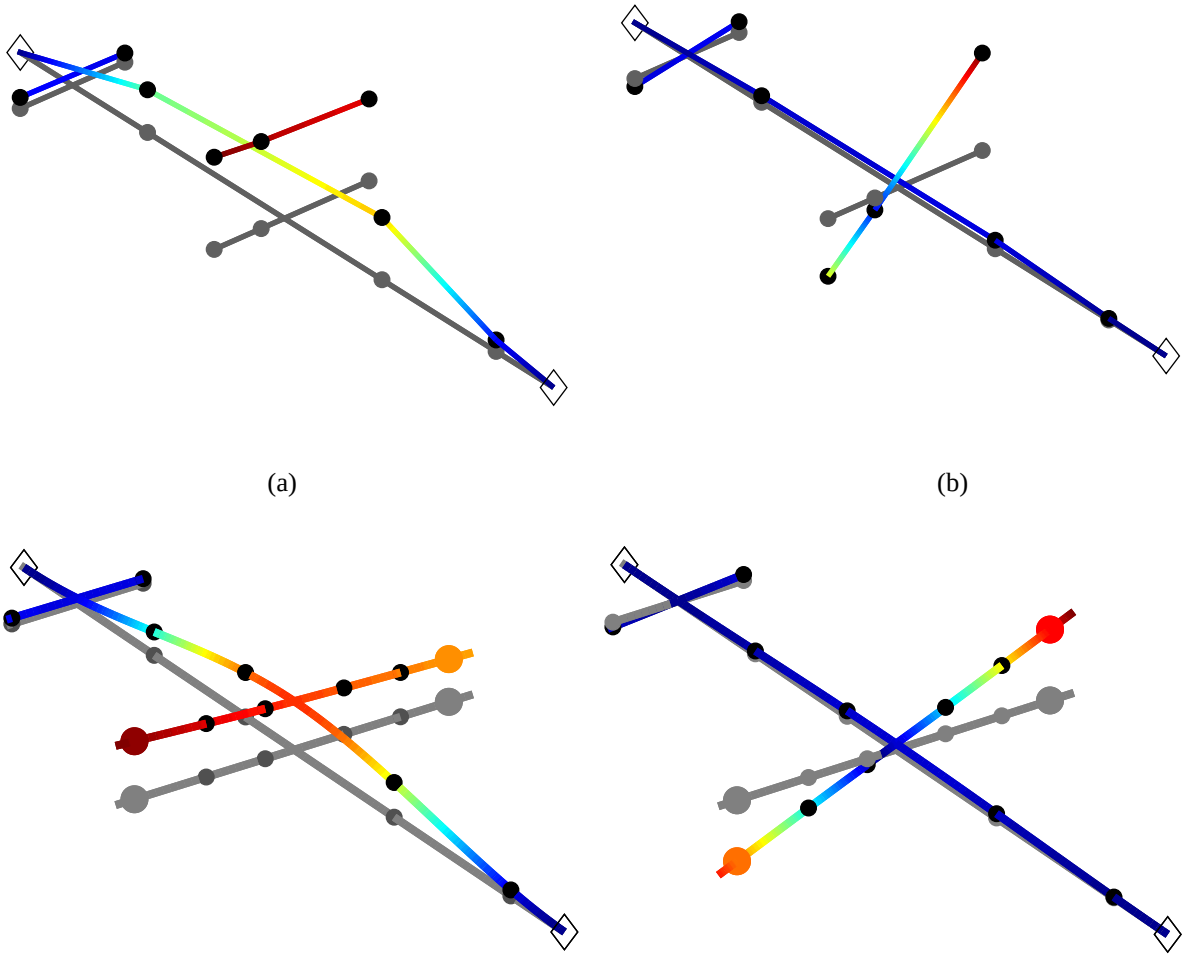

(a) (b)

(c) (d)

Fig. 18. Linear mode shapes of the test structure. The first two plots show (a) first bending mode and (b) first torsional mode extracted from the eight measured channels; the last two plots show (c) first bending mode and (d) first torsional mode of the updated finite-element model with 1050 DOFs. Grey curves denote the un-deformed structure, and black dots denote the locations of accelerometers.

$$\mathrm{MAC} = \begin{bmatrix} 0.9994 & 0.0763 \\ 0.0748 & 0.9993 \end{bmatrix} \tag{35}$$

Note that the first mode is not pure bending and the second mode is also not pure torsion due to the slightly asymmetrical effects. We now perform the linear expansion using Eqs. (14)-(16), and the first two finite-element mode shapes are used to fit the measured mode shapes, respectively. The transformation matrix in Eq. (15) is obtained as:

$$\mathbf{T} = \begin{bmatrix} 1.0016 & 0 \\ 0 & 1.0551 \end{bmatrix} \tag{36}$$

The mode shapes in the unmeasured region are now expanded by substituting Eq. (36) into Eq. (16), and subsequently, the expanded FRFs can be computed using Eq. **(9)**. Fig. 19 depicts expanded FRFs at two 'unmeasured' points (at the location of Acc. 4 and Acc. 8) obtained using Eq. (16). Note that these two points are measured during the experiment but not used in the analysis; they are only reserved to examine the expanded results. As can be seen from Fig. 19 that the linear expanded FRFs agree well with their true values.

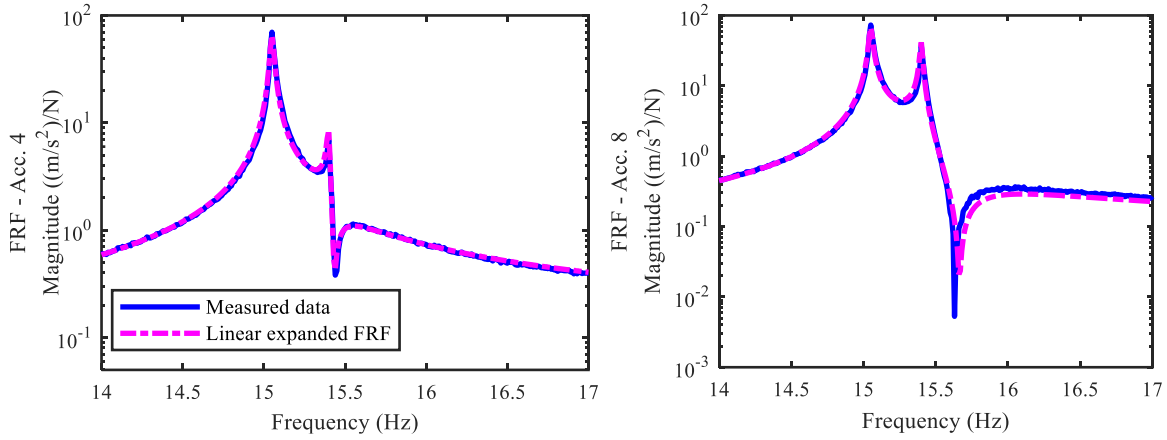

Fig. 19. Comparison of measured data and linear expanded FRFs at: (a) Acc. 4 on the main beam and (b) Acc. 8 on the cross-beam.

4.4. Nonlinear response expansion (Step 3-2)

We now investigate the dynamics of the diesis-like structure using high-amplitude stepped-sine tests with forcing levels of 0.5 N, 1 N, 2 N and 2.5 N. Fig. 20 shows the responses measured from two representative measured channels: Acc. 3 on the main beam and Acc. 7 on the cross-beam. It is clearly seen that the responses exhibit nonlinear behaviour when subjected to higher amplitude forcing, with jumps present at the 1.0 N, 2.0 N and 2.5 N excitation levels.

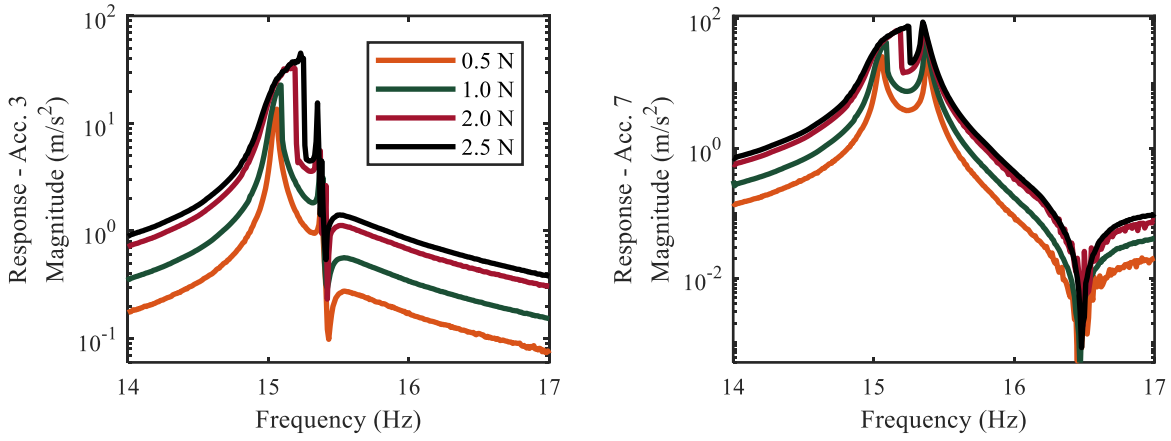

(a) (b)

Fig. 20. Measured nonlinear responses (forward sweep) using different levels of stepped-sine inputs at two representative locations: (a) Acc. 3 on the main beam and (b) Acc. 7 on the cross-beam.

The measured responses are then projected to the linear modes using Eq. (27). As shown in Fig. 21, the first mode demonstrates strong hardening and the second mode shows slightly softening with the increase of input forcing levels.

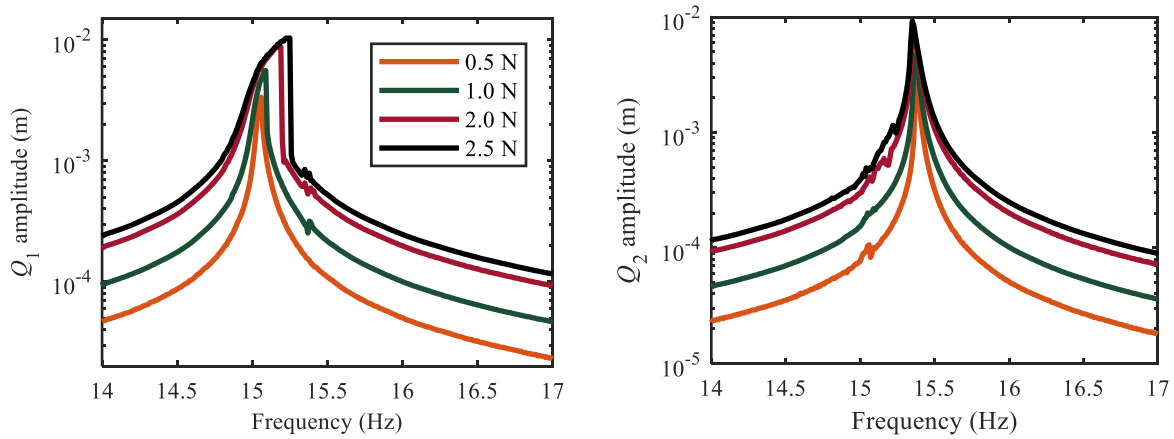

(a) (b)

Fig. 21. Projections of the measured responses to the linear modal domain: (a) first mode and (b) second mode.

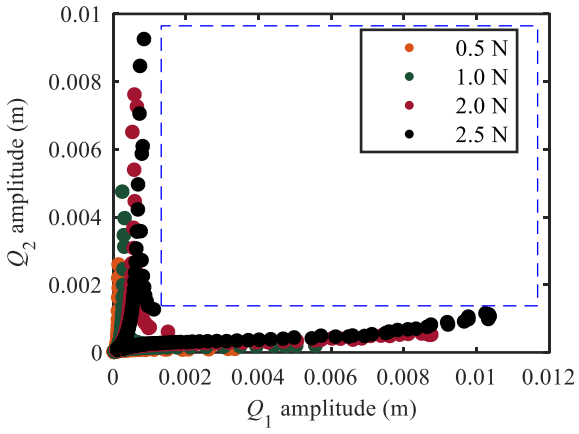

Fig. 22. Interaction map of the modes observed using high-amplitude testing.

Fig. 22 depicts the amplitude of both modes at each frequency point; it can be seen that the two modes are not significantly coupled and no significant internal resonances are observed. Therefore, the characterisation of the two nonlinear modes is further investigated using the Equivalent Dynamic Stiffness mapping technique [20,33], where the measured data is fitted with a series of basis functions for each mode. Detailed discussions of how to choose the basis functions to non-parametrically characterise the model can be found in [33]. Here, we consider a quadratic and a cubic nonlinear stiffness term for the first mode and a quadratic nonlinear stiffness term for the second mode, and a quadratic term for each modal damping, i.e., the model is fitted with Eqs. (37) and (38).

$$\ddot{q}_1 + 2\xi_1\omega_{r_1}\left(1+\rho_{c_1}|q_1|\right)\dot{q}_1 + \omega_{r_1}^2 q_1 + k_{21}q_1|q_1| + k_{31}q_1^3 = \boldsymbol{\phi}_1^{\mathrm{T}}\boldsymbol{p} \tag{37}$$

$$\ddot{q}_2 + 2\xi_2\omega_{r_2}\left(1+\rho_{c_2}|q_2|\right)\dot{q}_2 + \omega_{r_2}^2 q_2 + k_{22}q_2|q_2| = \boldsymbol{\phi}_2^{\mathrm{T}}\boldsymbol{p} \tag{38}$$

where ξ_1 and ξ_2 are modal damping ratios, ω_{r_1} and ω_{r_1} are natural frequencies from the linear experimental modal analysis; they are listed in Table 6. ρ_{c_1} and ρ_{c_2} are quadratic damping ratios. k_{21} and k_{31} are quadratic and cubic stiffness terms for the first mode, respectively. k_{22} is the quadratic stiffness term for the second mode.

Fig. 23 depicts the projections of the equivalent dynamic stiffness points and the fitted curves. The identified nonlinear coefficients for this structure are given in Table 7.

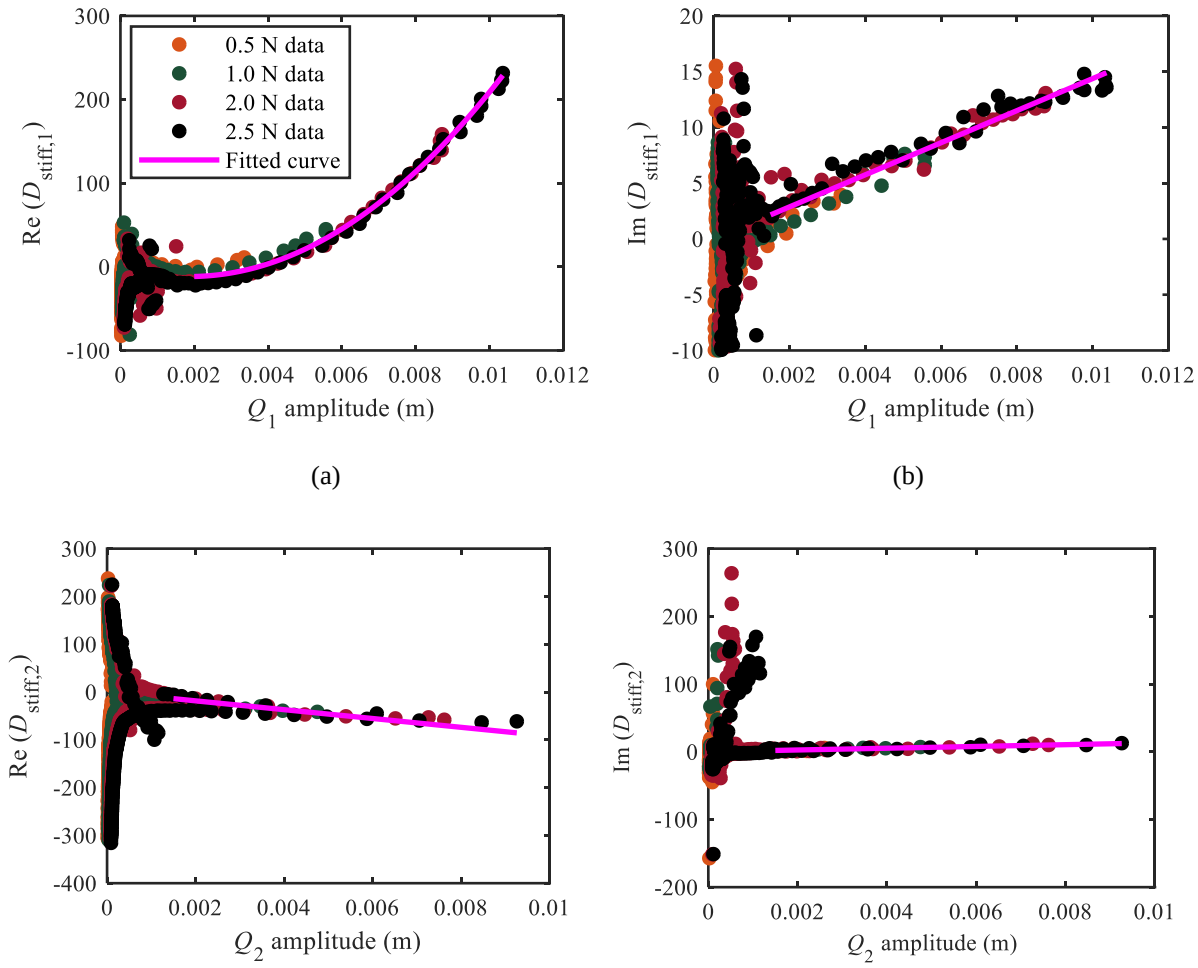

Fig. 23. Projections of the modal equivalent dynamics stiffness: (a) $\mathrm{Re}\left(D_{\mathrm{stiff},1}\right)-\left|Q_1\right|$ plane and (b) $\mathrm{Im}\left(D_{\mathrm{stiff},1}\right)-\left|Q_1\right|$ plane for the first mode; (c) $\mathrm{Re}\left(D_{\mathrm{stiff},2}\right)-\left|Q_2\right|$ plane and (d) $\mathrm{Im}\left(D_{\mathrm{stiff},2}\right)-\left|Q_2\right|$ plane for the second mode.

Table 7

Identified nonlinear coefficients for the asymmetrical diesis-like structure.

	Nonlinear stiffness		Nonlinear damping
	Quadratic term	Cubic term	Quadratic term
Mode 1	$k_{21}=-1.4665\times10^{4}\left(\mathrm{N/m^2}\right)$	$k_{31}=4.4417\times10^{6}\left(\mathrm{N/m^3}\right)$	$k_{c_1}=8.9546\times10^{1}\left(\mathrm{m^{-1}}\right)$
Mode 2	$k_{22}=-1.0879\times10^{4}\left(\mathrm{N/m^2}\right)$	N/A	$k_{c_2}=1.3022\times10^{2}\left(\mathrm{m^{-1}}\right)$

Next, Eqs. (37) and (38) are solved using the measured input force levels and the synthesised values are calculated using Eq. (24); these synthesised values are then compared to the measured data shown in Fig. 24 at three representative locations (Acc. 1, Acc. 5, Acc. 9 and Acc. 10). As can be seen that the synthesised FRFs using identified nonlinear coefficients achieve good accuracy with the measured data around resonances, which validates our identified results of the nonlinear coefficients.

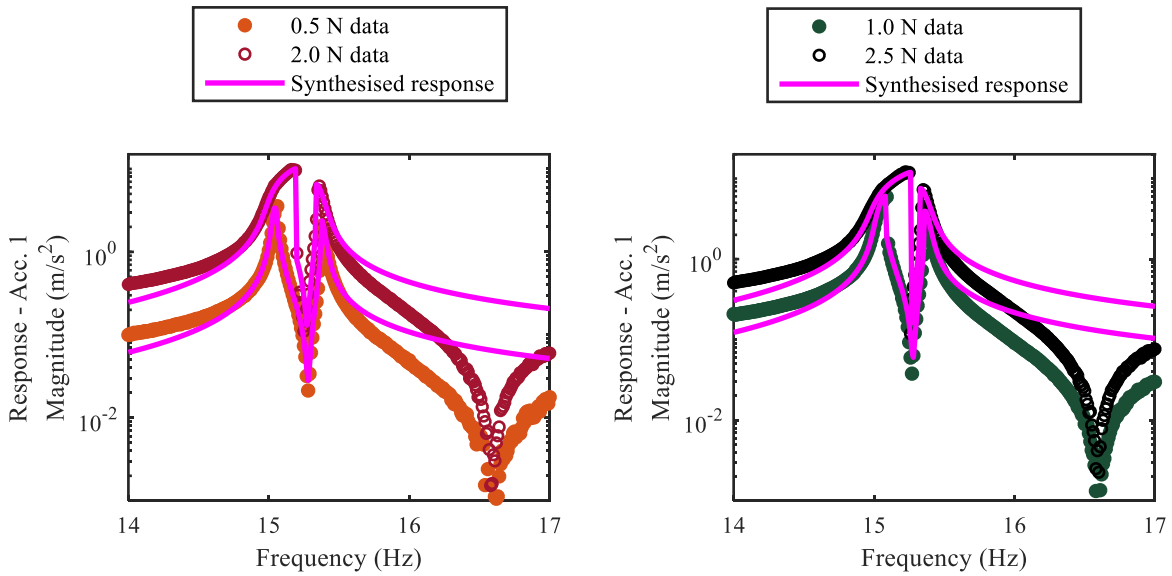

(a)

(b)

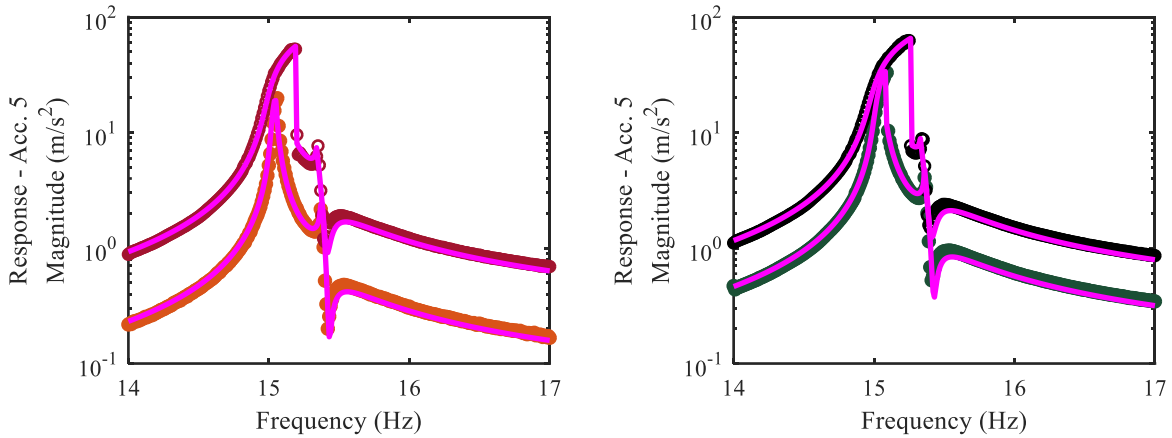

(c)

(d)

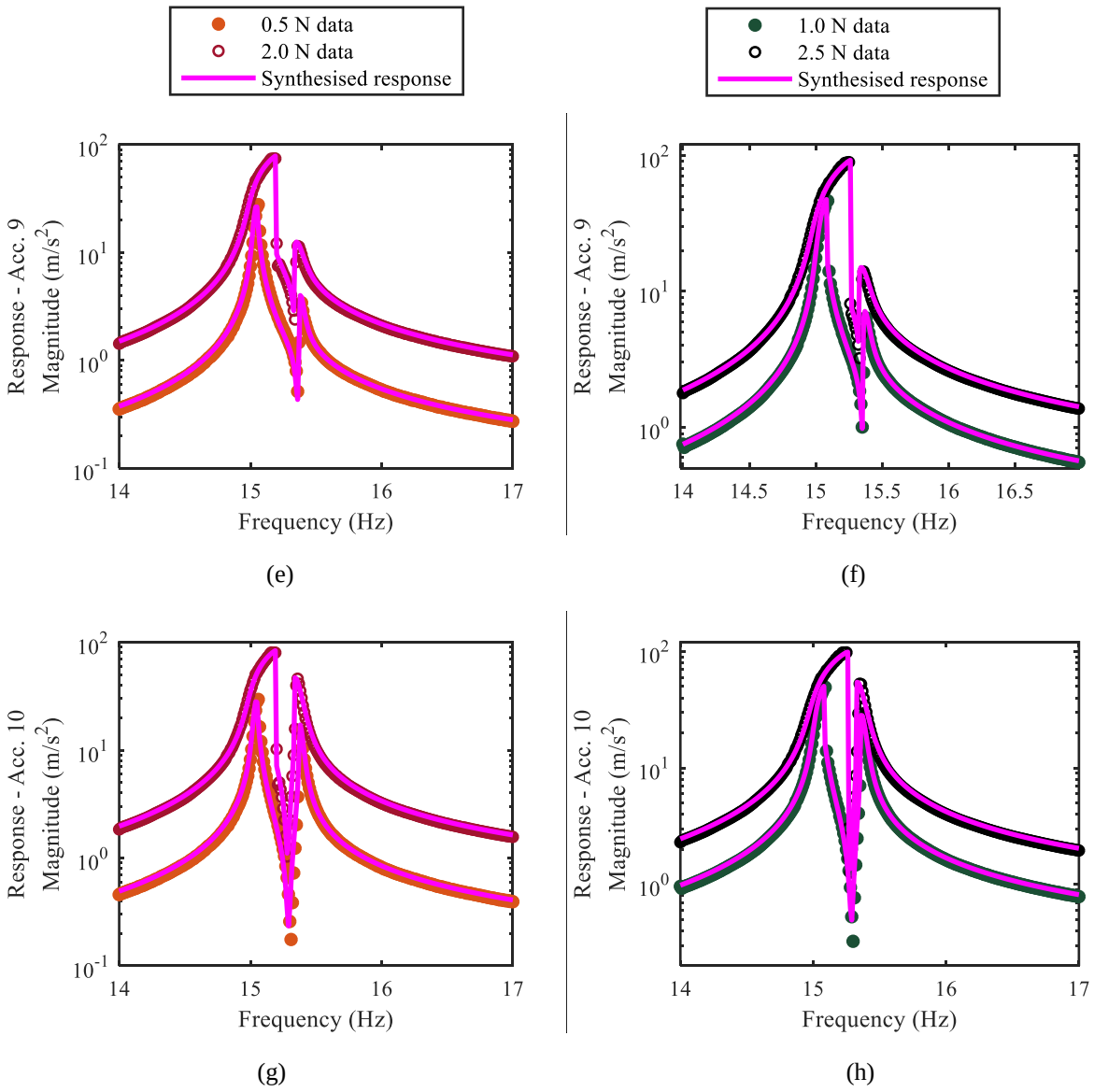

Fig. 24. Comparison between measured nonlinear response data and synthesised responses using identified nonlinear coefficients, where (a) and (b) show responses of Acc. 1; (c) and (d) depict responses of Acc. 5; (e) and (f) illustrate responses of Acc. 9; (g) and (h) are responses of Acc. 10.

After validation of the model, we then perform the expansion for the 'unmeasured' DOFs (Acc. 4 and Acc. 8). Recall that we measured these locations in the tests but the data were not used in the expansion; they are reserved for validation of the expanded results. Fig. 25 depicts a comparison of the expanded responses and measured data at positions where Acc. 4 and Acc. 8 are placed. It shows that the nonlinear expansion estimates the responses of the 'unmeasured' DOFs with good accuracy.

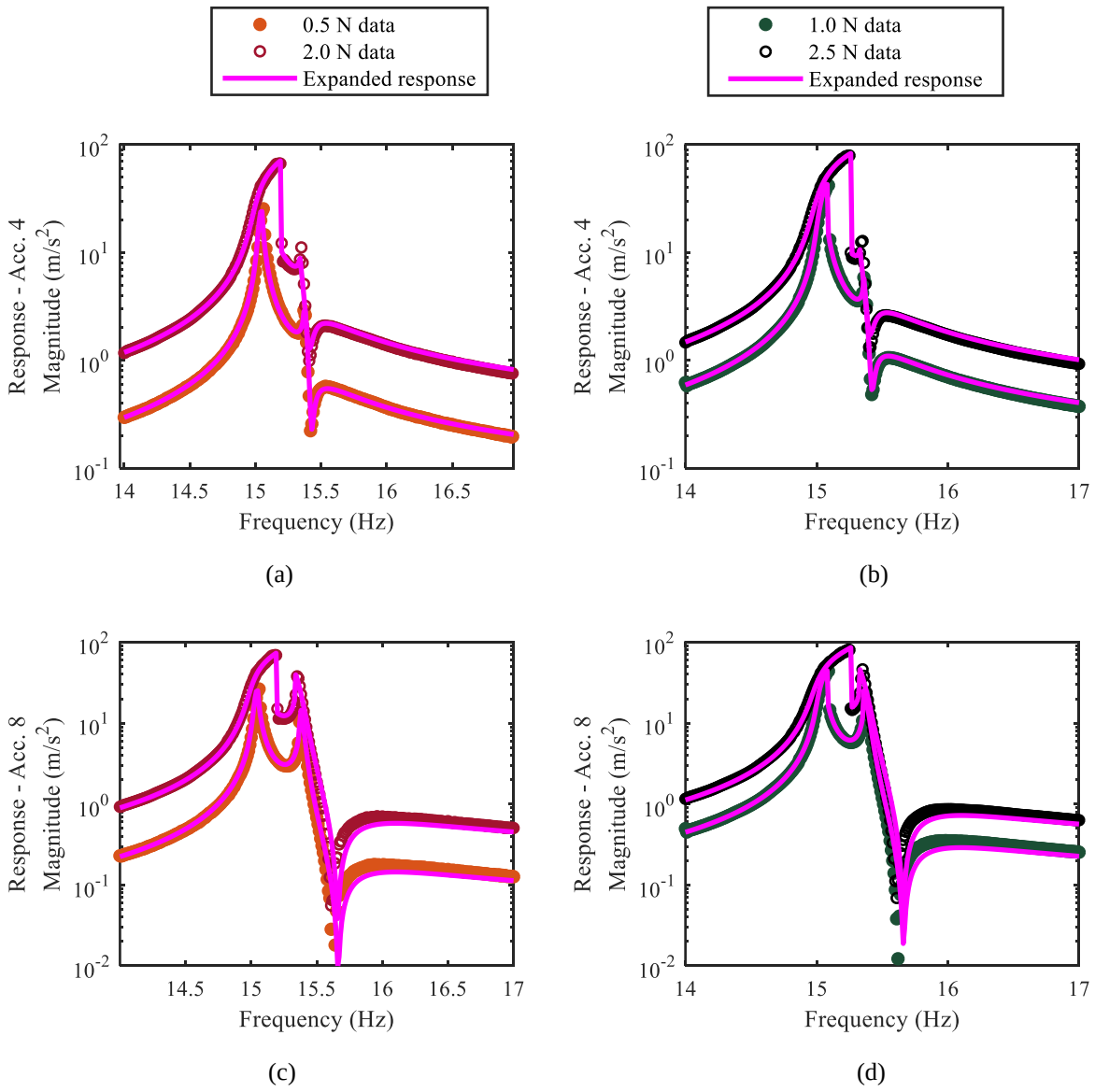

Fig. 25. Comparison between measured response data and expanded responses using identified nonlinear coefficients, where (a) and (b) show responses of Acc. 4; (c) and (d) depict responses of Acc. 8.

The final step is to verify the expansion technique by using it to predict responses at a new input force level and perform a measurement to demonstrate the accuracy of the predicted results. Here, it is demonstrated by examining the accuracy of predicted responses at 'unmeasured' locations (Acc. 4 and Acc. 8) using an 'unmeasured' forcing level - 1.5 N input. Note again that the data using 1.5 N input force were not included in previous expansion process; they are also reserved only for the purpose of validation here. Fig. 26 depicts a comparison of the predicted responses and measured data. It shows that the predicted responses agree well with the measured data at 'unmeasured' locations (Acc. 4 and Acc.

8) and 'unmeasured' input level (1.5 N). Note also that the forcing level in prediction is below the maximum forcing level used in the tests.

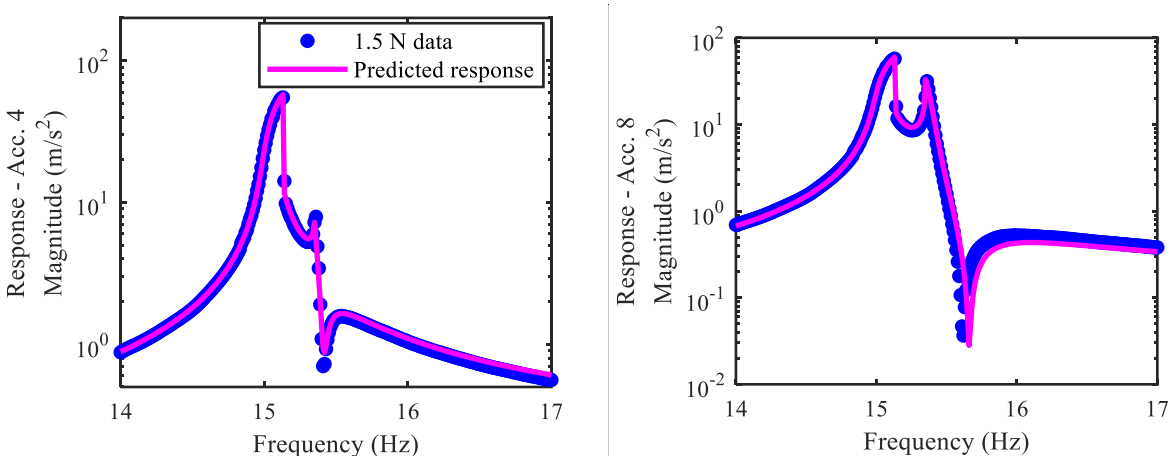

(a) (b)

Fig. 26. Comparison of measured response data and predicted responses at: (a) Acc. 4 on the main beam and (b) Acc. 8 on the cross-beam using a 1.5 N input force.

5. Conclusions and future work

This paper presents a novel strategy to estimate unmeasured responses of a structure with localised or distributed nonlinearities. The strategy starts with a linear experimental modal analysis, where the underlying linear modal properties are estimated using low-amplitude testing. Then the nonlinear responses, recorded from high-amplitude testing, are correlated with the measured underlying linear dynamics to extract the residuals, and subsequently, the nonlinear coefficients are estimated. Finally, the unmeasured nonlinear responses are expanded using the modal properties from linear experimental analysis and estimated nonlinear coefficients. Demonstrations and discussions of this strategy using firstly a numerical two-beam example and then an experimental diesis-like structure are presented. It is shown by both numerical and experimental examples that the nonlinear responses at unmeasured locations can be expanded with good accuracy, and the predicted responses at input forcing levels that were not used in the expansion can match well with the measured data.

A potential limitation of current work is that we consider the primary harmonic term to be dominant in the measured responses, which is only valid for nonlinear structures with moderate damping and no internal resonances. The sub- or super-harmonic resonances that may exist are not analysed here, and more complex nonlinear behaviours such as quasi-periodic or chaotic motions are also not within the scope of this paper. The proposed strategy also requires an FE model of the underlying linear system and assume that good agreement can be achieved using the mature linear model updating techniques. Future work could include a detailed analysis of the effects of the sensor placement to the accuracy of the expansion or extensions of this technique to investigate the optimal placement of the sensors for nonlinear structures.

Acknowledgement

The authors gratefully acknowledge the support provided by the EPSRC. X.W. is supported by the Engineering Nonlinearity programme grant EP/K003836/1 and S.A.N. by fellowship EP/K005375/1. As an EPSRC funded project, the data is openly available at DOI (to be presented on acceptance).

References

1. Göge, Dennis, Marc Böswald, Ulrich Füllekrug, and Pascal Lubrina. Ground Vibration Testing of Large Aircraft–State-of-the-Art and Future Perspectives. 25th International Modal Analysis Conference. 2007.
2. Goge, D., Fuellekrug, U., Sinapius, M., Link, M., & Gaul, L. Advanced test technique for identification and characterization of nonlinearities of aerospace structures. AIAA Journal 43.5 (2005): 974-986.
3. Ahlquist, Javier Rodríguez, José Martinez Carreño, Héctor Climent, Raúl de Diego, and Jesús de Alba. Assessment of nonlinear structural response in A400M GVT. Structural Dynamics, Volume 3. Springer, New York, NY, 2011. 1147-1155.
4. Noël, J. P., Renson, L., & Kerschen, G. Complex dynamics of a nonlinear aerospace structure: experimental identification and modal interactions. Journal of Sound and Vibration 333.12 (2014): 2588-2607.

5. A. Calvi, N. Roy, Spacecraft mechanical loads analysis handbook. ESA Requirements and Standards Division, Noordwijk, The Netherlands, 2013.
6. Vakakis, A. F., Bergman, L. A., McFarland, D. M., Lee, Y. S., & Kurt, M. Current efforts towards a non-linear system identification methodology of broad applicability. Proceedings of the Institution of Mechanical Engineers, Part C: Journal of Mechanical Engineering Science 225.11 (2011): 2497-2515.
7. Neild, S. A., Champneys, A. R., Wagg, D. J., Hill, T. L., & Cammarano, A. The use of normal forms for analysing nonlinear mechanical vibrations. Phil. Trans. R. Soc. A 373.2051 (2015): 20140404.
8. Noël, J. P., & Kerschen, G. Nonlinear system identification in structural dynamics: 10 more years of progress. Mechanical Systems and Signal Processing 83 (2017): 2-35.
9. Ewins, D. J., B. Weekes, and A. delli Carri. Modal testing for model validation of structures with discrete nonlinearities. Phil. Trans. R. Soc. A 373.2051 (2015): 20140410.
10. Ewins, D. J. Exciting vibrations: the role of testing in an era of supercomputers and uncertainties. Meccanica 51.12 (2016): 3241-3258.
11. Friswell, M. I., & Penny, J. E. T. Updating model parameters from frequency domain data via reduced order models. Mechanical Systems and Signal Processing 4.5 (1990): 377-391.
12. Avitabile, P., and J. O'callahan. Frequency response function expansion for unmeasured translation and rotation dofs for impedance modelling applications. Mechanical Systems and Signal Processing 17.4 (2003): 723-745.
13. Chen, H. P. Mode shape expansion using perturbed force approach. Journal of Sound and Vibration 329.8 (2010): 1177-1190.
14. Friswell M, Mottershead J E. Finite element model updating in structural dynamics [M]. Springer Science & Business Media, 1995.
15. Noël, J. P., & Kerschen, G. Frequency-domain subspace identification for nonlinear mechanical systems. Mechanical Systems and Signal Processing, 40(2013):701-717.
16. Noël, J. P., Marchesiello, S., & Kerschen, G. (2014). Subspace-based identification of a nonlinear spacecraft in the

time and frequency domains. Mechanical Systems and Signal Processing, 43(1-2), 217-236.

17. Peter, S., Scheel, M., Krack, M., & Leine, R. I. Synthesis of nonlinear frequency responses with experimentally extracted nonlinear modes. Mechanical Systems and Signal Processing 101 (2018): 498-515.

18. Göge, D. Automatic updating of large aircraft models using experimental data from ground vibration testing. Aerospace science and technology 7.1 (2003): 33-45.

19. Wang, X., Khodaparast, H. H., Shaw, A. D., Friswell, M. I., & Zheng, G. Localisation of local nonlinearities in structural dynamics using spatially incomplete measured data. Mechanical Systems and Signal Processing 99 (2018): 364-383

20. Wang, X., Thomas L. Hill, Simon A. Neild, Shaw, A. D, Khodaparast, H. H., M. I. Friswell. Model updating technique for structures with localised nonlinearities using frequency response measurements. Mechanical Systems and Signal Processing 100 (2018): 940-961.

21. K. Worden and G.R. Tomlinson. Nonlinearity in Structural Dynamics: Detection, Identification and Modelling. Institute of Physics Publishing, Bristol, UK, 2001.

22. Ewins, D. J. Modal testing: theory and practice. Letchworth: Research studies press. 1984.

23. Peeters, B., Lau, J., Lanslot, J., & Auweraer, H. V. D. Automatic Modal Analysis-Myth or Reality?. Sound and Vibration 42.3 (2008): 17.

24. Peeters, B., Lowet, G., Van der Auweraer, H., & Leuridan, J. A new procedure for modal parameter estimation. Sound and Vibration 38.1 (2004): 24-29.

25. Brown, D. L., Allemang, R. J., Zimmerman, R., & Mergeay, M. Parameter estimation techniques for modal analysis. No. 790221. SAE Technical paper, 1979.

26. Krauss, Thomas P., Loren Shure, and John N. Little. Signal Processing Toolbox for use with MATLAB. 1994.

27. Lee, Y. S., Vakakis, A. F., Bergman, L. A., McFarland, D. M., & Kerschen, G. Suppressing aeroelastic instability using broadband passive targeted energy transfers, part 1: theory. AIAA Journal 45.3 (2007): 693.

28. Ehrhardt, D. A., Neild, S. A., & Cooper, J. E. Experimental and numerical investigation of the nonlinear

bending-torsion coupling of a clamped-clamped beam with centre masses. Nonlinear Dynamics, Volume 1. Springer, Cham, 2016. 97-106.

29. Ehrhardt, D. A., & Allen, M. S. Measurement of nonlinear normal modes using multi-harmonic stepped force appropriation and free decay. Mechanical Systems and Signal Processing 76 (2016): 612-633.
30. Alijani, F., Amabili, M., Balasubramanian, P., Carra, S., Ferrari, G., & Garziera, R. Damping for large-amplitude vibrations of plates and curved panels, Part 1: Modeling and experiments. International Journal of Non-Linear Mechanics 85 (2016): 23-40.
31. Amabili, M., Alijani, F., & Delannoy, J. Damping for large-amplitude vibrations of plates and curved panels, part 2: Identification and comparisons. International Journal of Non-Linear Mechanics 85 (2016): 226-240.
32. Ehrhardt, D. A., Allen, M. S., Beberniss, T. J., & Neild, S. A. Finite element model calibration of a nonlinear perforated plate. Journal of Sound and Vibration 392 (2017): 280-294.
33. Wang, X., and Zheng G. T. Equivalent Dynamic Stiffness Mapping technique for identifying nonlinear structural elements from frequency response functions. Mechanical Systems and Signal Processing 68 (2016): 394-415.
34. B. Peeters, W. Hendricx, J. Debille, H. Climent. Modern solutions for ground vibration testing of large aircraft. Sound and Vibration, 43 (2009): 8-15
35. Renson, L, Ehrhardt, DA, Barton, DA, Neild, SA & Cooper, JE. Connecting nonlinear normal modes to the forced response of a geometric nonlinear structure with closely spaced modes. Proceedings of ISMA 2016 - International Conference on Noise and Vibration Engineering and USD2016 - International Conference on Uncertainty in Structural Dynamics. K U Leuven, (2016) 2775-2784.